IJIE

UTHM Penerbit

INTERNATIONAL JOURNAL OF INTEGRATED ENGINEERING
ISSN: 2229-838X e-ISSN: 2600-7916

Vol. 18 No. 3 (2026) 63-88
https://publisher.uthm.edu.my/ojs/index.php/ijie

Numerical Investigation of Defect Severity in Double-Slope 16MnR Steel Cracked Pipes with Uniform Corrosion Using the XFEM-Level Set Method

Houda Salmi[1]*, Houda Lifi[1], Khalid El Had[2], Abdelilah Hachim[2], Amal Lamati[2]

[1] *Mathematics, Computer Science, and Communication Systems Laboratory, National School of Applied Science of Safi, Cadi Ayyad University, Sidi Bouzid, BP 63, Safi 46000, MOROCCO*
[2] *Hassan II University of Casablanca (UH2C), National Higher School of Electricity and Mechanics, Laboratory of Mechanics, Engineering and Innovation, Higher Institute of Maritimes Studies, Km 8 Route El Jadida, B.P 5366 Maarif Casablanca 20100, MOROCCO*

*Corresponding Author: h.salmi@uca.ac.ma
DOI: https://doi.org/10.30880/ijie.2026.18.03.005

Article Info

Received: 22 September 2025
Accepted: 13 December 2025
Available online: 30 April 2026

Keywords

Double slopes, corrosion, pressurized pipelines, level set-XFEM, CASTEM code, 16MnR steel

Abstract

This study presents a numerical investigation into the severity of semi-elliptical surface cracks in 16MnR steel pipes featuring double-slope thickness transitions and subjected to uniform corrosion under internal pressure. The analysis employs a coupled XFEM–Level Set approach integrated with a Fick-based corrosion model, implemented in the CASTEM platform using a mesh comprising 9,290 CUB8 elements and 200 enriched XC8R elements to accurately capture stress singularities near crack fronts. Model validation against ASME B31G analytical solutions confirms high fidelity, with deviations below 5% across crack depth-to-thickness ratios (a/t) from 0.1 to 0.8 and aspect ratios (a/c) ranging from 0.125 to 1. Simulations were conducted under representative industrial operating pressure. Results indicate that the primary thickness transition ratio (t_1/t) critically governs stress concentration: increasing t_1/t from 1.5 to 6 raises the stress intensity factor (K) at the deepest crack point from 20.4 to 105.9 MPa√m—surpassing the critical fracture toughness of 16MnR steel (90 MPa√m) and inducing localized plasticity. Conversely, as cumulative metal loss (t_c) rises from 0% to 60%, K decreases from 14.6 to 9.5 MPa√m due to crack tip blunting. These findings highlight that initial geometric discontinuity—not secondary corrosion-induced thinning—is the dominant factor controlling defect severity. The study thus offers a robust quantitative basis for structural integrity assessment and residual life prediction in corroded pressurized pipelines.

1. Introduction

Modern infrastructure depends much on pipelines, which are also crucial for the long-distance transit of gas and liquids. These pipelines, typically made of steel, are protected by coatings to limit both external and internal corrosion. Despite these precautions, corrosion remains one of the primary causes of structural degradation, jeopardizing safety and operational efficiency [1]. Among the several types of corrosion, uniform corrosion and especially pitting corrosion cause material loss dispersed throughout the whole surface [2].

There has been substantial research on pipeline integrity, focused on understanding the connections between material qualities, environmental conditions, and mechanical stresses [3]. Notable contributions include studies by Loïc Oger and Turnbull et al. [4,5] on environmentally induced crack initiation, and Ouglova et al. [6, 7] on the impact of rebar corrosion in reinforced concrete structures due to chloride ingress. However, predictive modeling still requires improvement, particularly for complex geometries and evolving defects, as many existing approaches rely on traditional numerical or experimental methods with inherent limitations.

The extended finite element method (XFEM), which does not require remeshing during crack propagation, has proven effective in simulating fracture evolution. When combined with level set techniques, XFEM enables accurate tracking of crack fronts in complex configurations [8, 9]. Nevertheless, its application to corroded pressurized pipes—especially those with double-slope thickness transitions and variable defect shapes—remains largely unexplored.

To address this gap, this study proposes an advanced numerical framework based on the coupling of the XFEM method, Level Set techniques, and a Fick-based corrosion model [6,10], all implemented within the CASTEM 2025 software. The objective is to assess the severity of semi-elliptical surface cracks in 16MnR steel pipes featuring dual thickness transitions under uniform internal corrosion. The methodology follows a systematic approach:

A cylindrical pipe under internal pressure is modeled with three distinct wall thickness zones: main zone (t), first transition (t_1), and second transition (t_2).

Due to geometric and mechanical symmetry, only half of the pipe is simulated, with a semi-elliptical external crack introduced at the base of the first thickness transition—where stress concentration is expected to be highest. Symmetry boundary conditions are applied to ensure equilibrium.

Uniform corrosion is modeled as a diffusion process governed by Fick's law [10], describing the spatiotemporal evolution of corrosive agent concentration. Wall thinning is computed independently in each zone based on local concentration, enabling non-uniform degradation.

The XFEM-Level Set coupling allows precise crack representation without remeshing: the Level Sets implicitly define the crack location via scalar functions (Φ for crack plane, ψ for crack front), while XFEM enriches displacement fields near the crack using Heaviside and asymptotic functions.

Internal pressure varies from 10 to 50 bar. Elastic equilibrium equations are solved numerically, with focus on circumferential stress—the dominant stress component in pressurized pipes. Strain-stress relationships are governed by Hooke's generalized law.

Defect severity is evaluated through the Stress Intensity Factor (K), calculated using the G-theta method (J-integral) in CASTEM, suitable for elastic-plastic behavior. K is assessed at two critical points: the deepest point and the surface point of the crack and compared to the critical threshold of 90–100 MPa$\sqrt{m}$ for 16MnR steel.

Before analysis of complex configurations, the model is validated against analytical solutions from the ASME B31G code for ultimate pressure prediction.

A parametric study investigates the influence of key variables: primary transition ratio (t_1/t), secondary transition ratio (t_2/t_1), slope angles (α_1, α_2), corrosion rate, and internal pressure. The variation of K is analyzed to identify the parameters most affecting defect severity.

This integrated approach provides a comprehensive framework for assessing structural integrity in corroded pipelines with complex geometries, offering new insights into defect nocivity and supporting improved life prediction strategies.

2. Corrosion Model Coupled with the XFEM Method and LEVELSET

2.1 XFEM-LEVEL SETS Formulation

In the XFEM, the conventional finite element approximation is locally enhanced to account for the presence of discontinuities. At a given node i, the displacement approximation U is expressed as shown in Eq. (1) [8]:

$$U(x) = \sum_{i \in N} N_i(x)\, u_i + \sum_{i \in N_d} N_i(x)(H(x) - H(x_i))a_i + \sum_{i \in N_p} [\, N_i(x)(\sum_{\alpha=1}^{4} (\beta_\alpha(x) - \beta_\alpha(x_i))\, b_i^\alpha)] \qquad (1)$$

N_i : standard finite element (FE) function of node i.

u_i: unknown of the standard finite element (FE) part at the node i.

N : set of all nodes in the domain.

$N_d \subset N$: nodal subset of the enrichment Heaviside function H(x), which is defined for those elements that are entirely cut by the crack surface:

Int. Journal of Integrated Engineering Vol. 18 No. 3 (2026) p. 63-88

$$H(x) = \{^{1 \quad if \quad \varphi(x)>0}_{-1 \quad otherwise} \tag{2}$$

$\varphi(x)$ is the normal level set.

a_i: unknown of the enrichment H (x) at node i , these nodes are surrounded by a square in Fig. 1.

$N_p \subset N$: nodal subset of the enrichment $\beta_{\alpha c}$, which is defined for those elements that are partly cut by the crack front. The crack tip is represented by four functions:

$$\{\beta_{\alpha_c}(r_c,\theta_c)\} = \{\beta_1,\beta_2,\beta_3,\beta 4\} = \left\{\sqrt{r}\,sin(\frac{\theta_c}{2}),\sqrt{r_c}\,cos(\frac{\theta_c}{2}),\sqrt{r_c}\,sin(\frac{\theta_c}{2})\,sin(\theta_c),\sqrt{r_c}\,cos(\frac{\theta_c}{2})\,sin(\theta_c)\right\} \tag{3}$$

Where $r_c = \sqrt{(\varphi^2 + \psi^2)}$and $\theta_c = tan^{-1}(\frac{\varphi}{\psi})$ with φ and ψ are respectively normal and tangential level sets.

b_i: unknown of the function β_{α_c}at node i (Fig. 1).

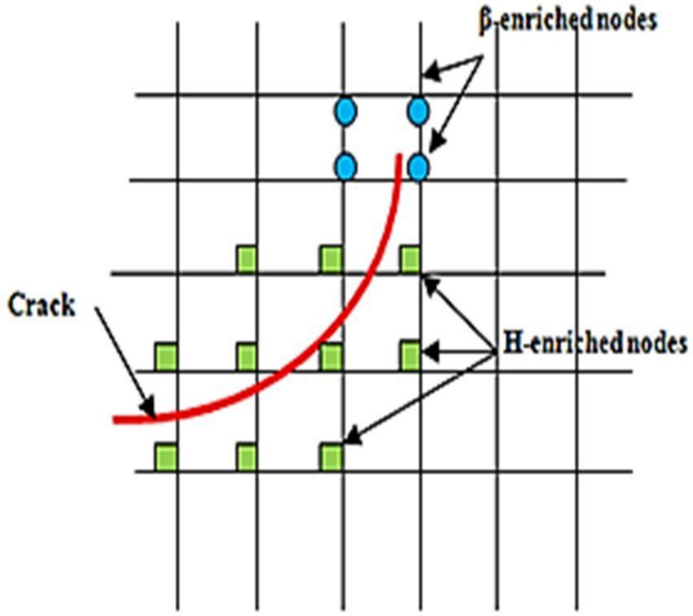

Fig. 1 *Enrichment Technique in XFEM [8]*

The level sets were defined [8] by computing them from the crack mesh. The function φ represents the separation between a point (x) and the crack surface, while (ψ) indicates the distance from a point (x) to the crack tip (Fig. 2). The functions (φ,ψ) describe the crack as defined by the Eq. (4):

$$x \in crack \Rightarrow \{^{\varphi(x)=0}_{\psi(x)\leq 0} with \ (|\nabla\psi| = |\nabla\varphi| = 1) \tag{4}$$

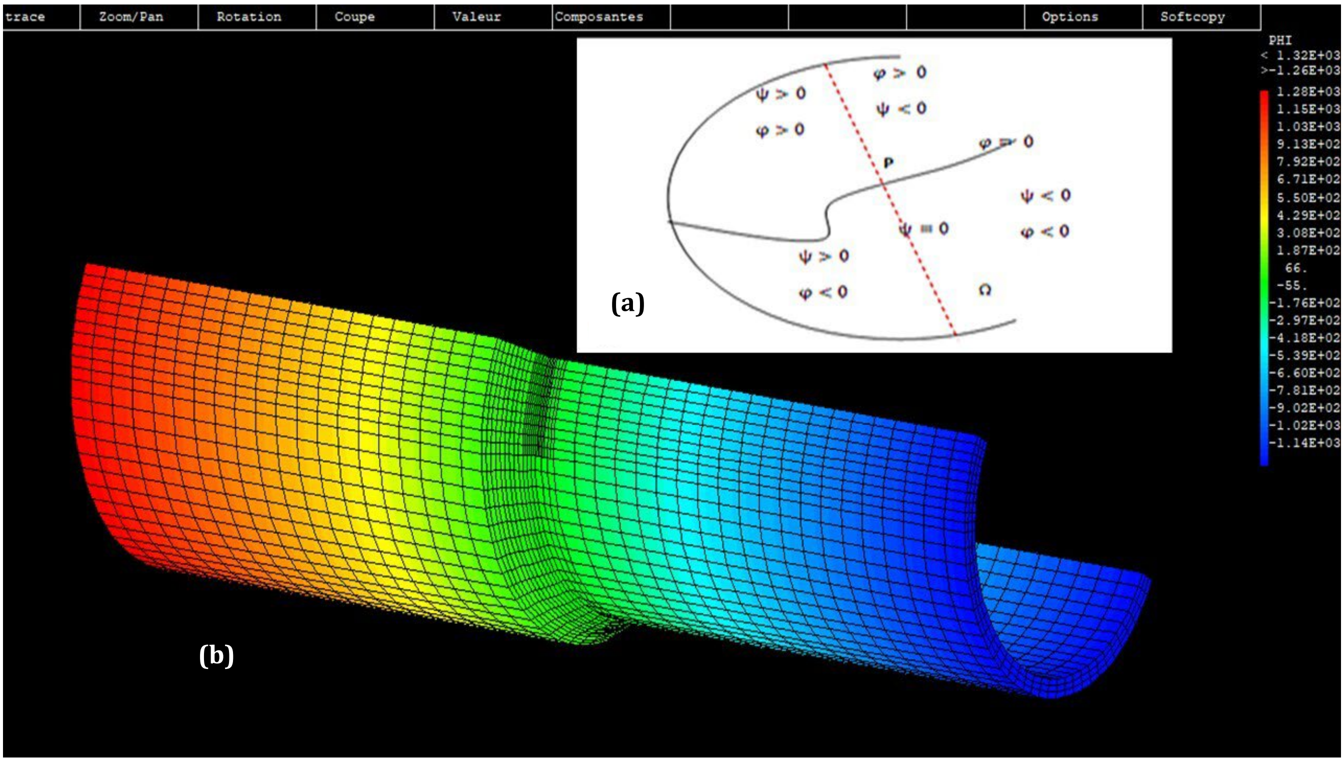

Fig. 2 *Crack representation in XFEM (a) Crack representation using Level Sets* $\boldsymbol{\varphi}$ *and* $\boldsymbol{\psi}$ *; (b) Normal level set simulation,* $\boldsymbol{\varphi}$

2.2 Governing Equations

This study considers a pipe with three regions of different thicknesses: t (main pipe),t_1 (transition 1), and t_2 (transition 2) (Fig. 3). The model geometry is cylindrical. Uniform corrosion will impact the reduction in thickness of these regions and, consequently, the deformation of the material under internal pressure.

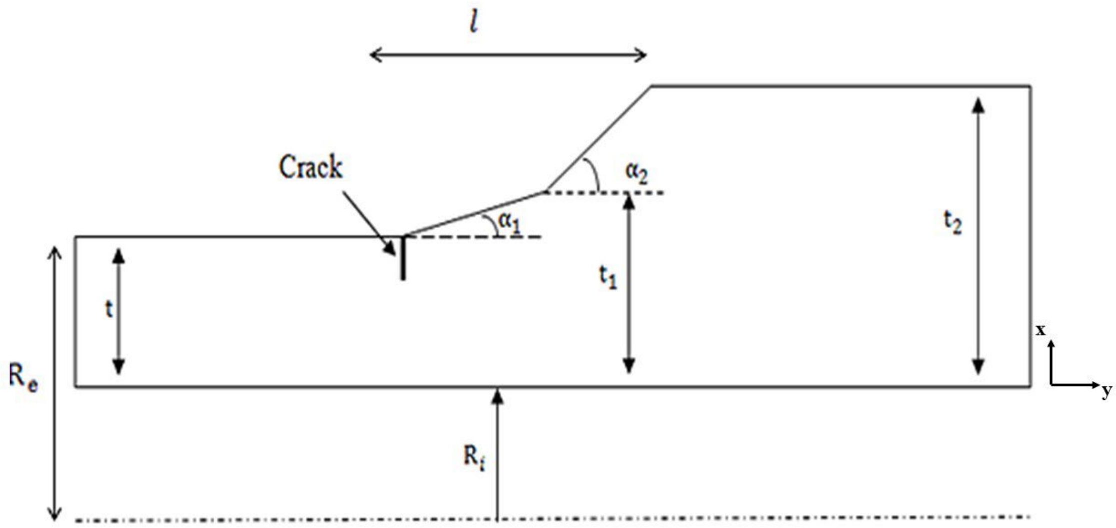

Fig. 3 *Pipe with thickness transition and double slopes*

The modeling of uniform corrosion in the pipe is based on Fick's law[10], where the concentration of the corrosive agent in the pipe material is given by the diffusion equation in Eq. (5):

$$\frac{\partial C(x,t_{im})}{\partial t_{im}} = D_{dif}\nabla^2 C(x,t_{im}) \tag{5}$$

$C(x, t_{im})$ is the concentration of the corrosive agent at position $x$at time t_{im}.
D_{dif} is the diffusion coefficient of the corrosive agent.
∇^2 is the Laplace operator, representing the diffusion in different spatial directions.

Boundary conditions for $C(x, t_{im})$: At the inner surface of the pipe, where $(x = 0)$: $C(0, t_{im}) = C_0$; C_0 represents the maximum concentration of the corrosive agent. At the outer surface of the pipe, a constant value is assumed for the concentration. $(x = t_2)$: $C(t_2, t_{im}) = C_1$.

Corrosion leads to a reduction in the thickness of the pipe walls. Assuming that the reduction in thickness in each region of the pipe (regions t, t_1 and t_2) is proportional to the concentration of the corrosive agent$C(x, t_{im})$. The corrosion rate is modeled by a corrosion rate (k) or (t_c), and the evolution of the thickness can be modeled by Eq. (6):

$$\frac{d}{dt}\begin{bmatrix} t(x, t_{im}) \\ t_1(x, t_{im}) \\ t_2(x, t_{im}) \end{bmatrix} = -k.\, C(x, t_{im}) \begin{bmatrix} 1 \\ 1 \\ 1 \end{bmatrix} \tag{6}$$

$t(x, t_{im})$: thickness in the first region t at time t_{im}.
$t_1(x, t_{im})$: thickness in the transition region t_1 at time t_{im}.
$t_2(x, t_{im})$: thickness in the transition region t_2 at time t_{im}.

Eq. (6) means that the reduction in thickness is calculated independently for each zone. This accounts for the possibility that $C(x, t_{im})$ and (k) vary from one zone to another.

The application of the XFEM method coupled with the level set allows for tracking the evolution of cracks that may propagate due to uniform corrosion. The level set represents the geometry of the crack or corroded zone as an implicit function. The normal level set function $\varphi(x, t_{im})$ (Section 1.2) is defined for each point in the geometry, and in this study, it represents the distance to the crack or corrosion front.

The variation of the function $\varphi(x, t_{im})$ over time t_{im} can be linked to the corrosion rate and the concentration of the corrosive agent through Eq. (7):

$$\frac{\partial \varphi(x, t_{im})}{\partial t_{im}} = -k.\, C(x, t_{im}) \tag{7}$$

Eq. (7) makes it possible to track the progression of corrosion and crack as a function of concentration $C(x, t_{im})$.

The force equilibrium (Eq. (8)) in a pressurized pipe is governed by the equations of elasticity. For a pipe subjected to internal pressure:

$$\nabla\sigma(x, t_{im}) + b(x, t_{im}) = 0 \tag{8}$$

Where $\sigma(x, t_{im})$ is the stress tensor. $b(x, t_{im})$ is the volumetric force vector.

For a pipe under internal pressure, there are three types of stress: the circumferential stress, acting in the circumferential (tangential) direction; the longitudinal stress, resulting from the effect of internal pressure on the ends of the pipeline; and the radial stress, acting in the radial direction. In this case, the study focuses on a long (effectively infinite) pipeline, either thick-walled or thin-walled, where the radial stress remains low and decreases linearly across the thickness [11]. Consequently, attention is restricted to the circumferential stress expressed in Eq. (9):

$$\begin{cases} \sigma_\theta = \dfrac{P\, R_i^2}{t(x, t_{im})} \\ \sigma_{\theta_1} = \dfrac{P\, R_i^2}{t_1(x, t_{im})} \\ \sigma_{\theta_2} = \dfrac{P\, R_i^2}{t_2(x, t_{im})} \end{cases} \tag{9}$$

P is the internal pressure. t, t_1, t_2 are the thicknesses in the corresponding regions (Fig. 3). R_i is the internal radius corresponding to each pipe zone. According to equations Eqs. (8-9), the force equilibrium on the pipe will also be influenced by the variations in thickness due to corrosion.

The deformation in the material is related to the stresses by the generalized Hooke's law for elastic materials, taking into account the variations in thickness in each section of the pipe:

$$\varepsilon(x, t_{im}) = D.\sigma(x, t_{im}) \tag{10}$$

$\varepsilon(x, t_{im})$ is the strain tensor.D is the material stiffness matrix (Young's modulus and Poisson's ratio). Displac ements $U(x, t_{im})$ are related to the strain by Eq. (11):

$$U(x, t_{im}) = \int_0^{t_2} \varepsilon(x, t_{im}) dt \tag{11}$$

Initial conditions for the concentration of the corrosive agent and the initial thickness of the pipe are $(x = 0)$: $C(0, t_{im}) = C_0$,$(x = t_2)$: $C(t_2, t_{im}) = C_1$and $t(x, 0) = t, t_1(x, 0) = t_1, t_2(x, 0) = t_2$.

To solve the problem of a corroded pipe with a double thickness transition under internal pressure using the XFEM method and level set, it is necessary to formulate the equations in matrix form. An elastic region of the pip e subjected to surface forces is examined. such as pressure or displacement, and volumetric forces (Fig. 4). The ai m is to determine stress and strain at each point. These quantities are represented as tensors and formatted int matrices.

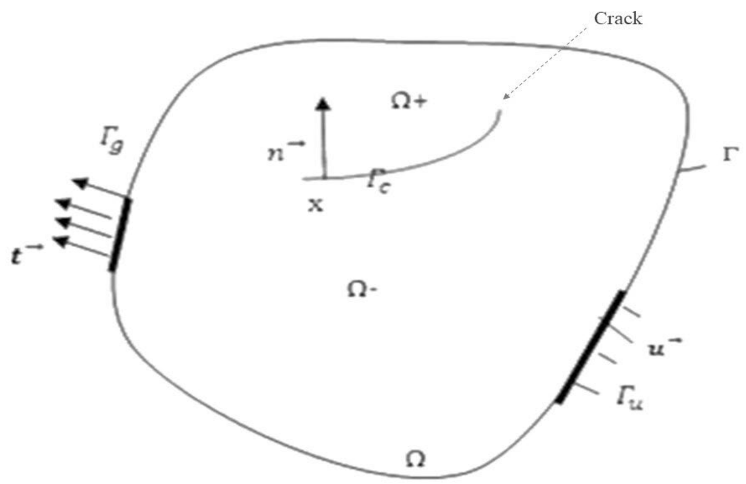

Fig. 4 *Crack in domain Ω*

Γ is the outer boundary of the domain Ω with $\Gamma = \Gamma_u \cup \Gamma_g$. The governing equations are expressed by Eqs. (12-1 6):

$$\nabla\sigma + b = 0 \quad or \quad \left(\sigma_{i\,j,j} + b_i\right) = 0, \;\; \Omega = \Omega^+ \cup \Omega^- \tag{12}$$

$$\sigma_{ij,j} n = t_{f_i} on \;\; \Gamma_g \tag{13}$$

$$U_i = u_i \;\; on \;\; \Gamma_u \tag{14}$$

$$\sigma_{ij,j} n = 0 \;\; on \;\; \Gamma_c \tag{15}$$

$$\varepsilon_{ij} = \frac{1}{2}(U_{i,j} + U_{j,i}) \tag{16}$$

Int. Journal of Integrated Engineering Vol. 18 No. 3 (2026) p. 63-88

$\Omega \in \mathbb{R}^3$ and $\vec{n}$ is a unit normal vector on the surface, b_i is the body force per unit volume.Γ_g, Γ_u and Γ_c are the traction, displacement, and crack boundaries, respectively. Eq. (12) represents the equilibrium equation, where σ_{ij}denotes the Cauchy stress tensor. Eqs. (13), (14), and (15) are derived from the equilibrium conditions on the surfaces, where t_{f_i} represents the tensile force applied to the given surface, and Udescribes the displacement field at any point on the solid's surface. Eq. (16) is a geometric relation that defines the strain under the assumption of small deformations, with ε_{ij}being the strain tensor at any point within the domain.

In numerical analysis, the goal is often to minimize the elastic potential energy by determining the optimal stresses and strains. The software Castem [12] solves Eq. (17):

$$K_{mat}U = f_{ext} \tag{17}$$

f_{ext} is the external force vector, and K_{mat} is the stiffness matrix:

$$K_{mat} = \int_{\Omega} B^T DBd\Omega \tag{18}$$

$$f_{ext} = \int_{\Omega} bd\Omega + \int_{\Gamma_g} t_{f_i} d\Gamma \tag{19}$$

Sub-matrices $K_{mat_{ij}}$ and $f_{i_{ext}}$ are derived by substituting the approximation functions defined in Eqs. (1), (3), (18), and (19):

$$K_{mat_{ij}} = \begin{pmatrix} K_{ij}^{uu} & K_{ij}^{ua} & K_{ij}^{ub} \\ K_{ij}^{au} & K_{ij}^{aa} & K_{ij}^{ab} \\ K_{ij}^{bu} & K_{ij}^{ba} & K_{ij}^{bb} \end{pmatrix} and \quad f_{iext}^{\hat{h}} = \{f_i^u\, f_i^a\, f_i^{b_1}\, f_i^{b_2}\, f_i^{b_3}\, f_i^{b_4}\}^T \tag{20}$$

The sub-matrices and vectors that appear in the foregoing Eq. (20) are given as:

$$K_{ij}^{ol} = \int_{\Omega} (B_i^o)^T D(B_j^l) d\Omega \quad w\hat{h}ere \quad o, l = a, u, b \tag{21}$$

$$f_i^u = \int_{\Omega} N_i\, b_i d\Omega + \int_{\Gamma_g} N_i\, t_i d\Gamma \tag{22}$$

$$f_i^a = \int_{\Omega} N_i\,(H(x) - H(x_i)) b_i d\Omega + \int_{\Gamma_g} N_i\,(H(x) - H(x_i)) t_i d\Gamma \tag{23}$$

$$f_i^{b\alpha} = \int_{\Omega} N_i\,(\beta_\alpha(x) - \beta_\alpha(x_i)) b_i d\Omega + \int_{\Gamma_g} N_i\,(\beta_\alpha(x) - \beta_\alpha(x_i)) t_i d\Gamma \quad w\hat{h}ere \;\; \alpha = 1,2,3,4 \tag{24}$$

N_i : standard finite element (FE) function of node i.
B_i: matrix of shape function derivatives, it is calculated at the Gauss points of each element.
Γ_g: traction boundary.

The discretized equation for uniform corrosion distribution according to Fick's law [10] in Eq. (5) is given by Eq. (25):

$$\frac{\partial C(x, t_{im})}{\partial t_{im}} = M^{-1} K_{co} C \tag{25}$$

Where M is the diffusion mass matrix. K_{co} is the thermal conductivity matrix (diffusion matrix). C is a vector of corrosion concentrations at the nodes in the three-dimensional space.

$$M_{ij} = \int_{\Omega} N_i(x) N_j(x) dx \tag{26}$$

$$K_{co_{ij}} = \int_{\Omega} \nabla N_i(x).\nabla N_j(x)dx \tag{27}$$

$$C = \begin{bmatrix} C_1(t_{im}) \\ C_2(t_{im}) \\ \cdot \\ \vdots \\ C_N(t_{im}) \end{bmatrix} \tag{28}$$

$$C(x, t_{im}) = \sum_i N_i(x, y, z)C_i(t_{im}) \tag{29}$$

In this study, the assessment of defect severity in a corroded and cracked pipe was conducted by evaluating the variations in Stress Intensity Factor values (SIF or K) modeled using the XFEM method.

Energy dissipated during an infinitesimal crack advancement presents the energy restitution rate (G). The G-theta method, implemented in the structural analysis software CASTEM 2025, provides an efficient means to calculate J-integral in cases involving elastic-plastic behavior. Notably, in purely elastic conditions, the J-integral is closely related to the energy release rate[12]. (K), is obtained from (G) through Eq. (30):

$$G = \frac{K^2}{E'} \quad with \quad E' = \frac{E}{(1-\vartheta^2)} \quad in \ \ plane \ \ strain \tag{30}$$

3. Structural Configuration

3.1 Applied Forces

Operating pressure, test pressure, and ultimate pressure are the three main pressure levels that pipelines must adhere to in accordance with the ASME B31G regulation. The nominal pressure at which the pipeline functions safely under typical service circumstances is known as the working pressure. The greater pressure utilized during inspection or commissioning to confirm the pipeline's structural soundness and leak-free condition is known as the test pressure.

A critical criterion for evaluating safety margins and the structural robustness of the material is the ultimate pressure, or the maximum pressure the pipeline can withstand before failure. Depending on the purpose of the research, different pressure levels are considered in pipeline analysis. The working pressure represents the typical operating circumstances under which the pipeline functions safely, ensuring that strains and deformations remain within permissible limitations. The structural integrity and leak-tightness of the pipeline are assessed using the test pressure. Since the ultimate pressure is the maximum pressure that the pipeline can withstand before collapsing, it is an essential parameter for evaluating safety margins and material resistance.

In the modified ASME B31G code[13], the ultimate pressure is given by Eq. (31):

$$P_{ult} = \frac{2(1.1\sigma_y)t}{D_{ext}} \left[\frac{1 - \frac{A_C}{A_{C_0}}}{1 - \frac{A_C}{A_{C_0}} \frac{1}{M}} \right] \tag{31}$$

A_C: longitudinal surface of the lost metal (Fig. 5).
A_{C_0}: original surface of the corroded area.
M : buckling factor expressed by Eq. (32):

$$M = \sqrt{1 + 0.62757 \frac{(2c)^2}{Dt} - 0.003375 \left(\frac{(2c)^2}{Dt} \right)^4} \tag{32}$$

The corrosion area is calculated by Eq. (33):

$$A_{C0} = 2ct \tag{33}$$

Int. Journal of Integrated Engineering Vol. 18 No. 3 (2026) p. 63-88

According to the corrosion defect length, the ASME B31G[13] standard adopts a parabolic or rectangular shape. In the case of a parabolic defect, A_c is given according to Eq. (34):

$$A_C = \frac{4}{3}ac \tag{34}$$

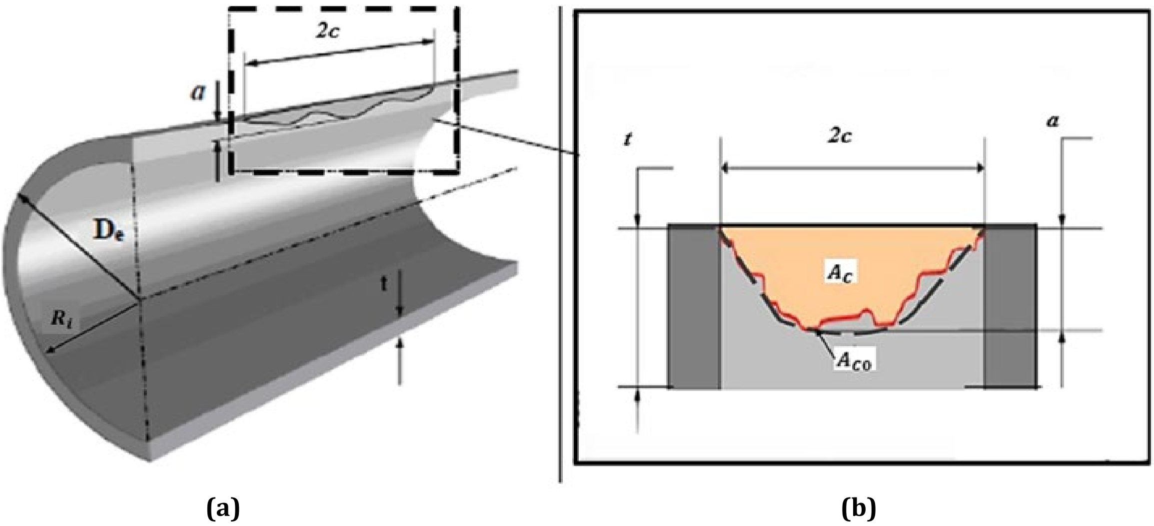

Fig. 5 *Straight pipe with a parabolic corroded defect (a) General view of the parabolic defect; (b) Geometrical detail of the corroded defect*

Ultimate pressure is calculated according to Eq. (31). The selected calculation pressure is significantly lower than the ultimate pressure to ensure the material remains in its elastic behavior. Numerical calculations were performed for a pressure of 10 bar, followed by an increase up to 40 bar.

The internal pressure of 15 bar was selected as the reference loading condition for numerical simulations, as it represents a typical operational pressure in industrial pressurized fluid transport systems [13]. This value lies between the nominal working pressure and the hydrostatic test pressure, enabling the assessment of the pipe's mechanical response within the elastic regime while approaching critical stress levels without triggering immediate plastic failure. Specifically:

For 16MnR steel, commonly used in petrochemical and thermal power installations, the standard operating pressure typically ranges between 10 and 20 bar, in accordance with ASME B31G guidelines [13].

Pressures of 10 or 15 bar thus represent realistic operational scenarios, ideal for investigating the influence of geometric parameters—such as thickness transitions—on stress concentration, while avoiding premature plastic deformation.

This pressure level also enables effective comparison of various corrosion and cracking scenarios, particularly when higher pressures (up to 40 bar) are applied to explore elastoplastic behavior (Fig. 6). Furthermore, this choice facilitates the numerical validation of the model, as it aligns with the pressure ranges commonly adopted in ASME-based analytical methods, where values are typically normalized within this range.

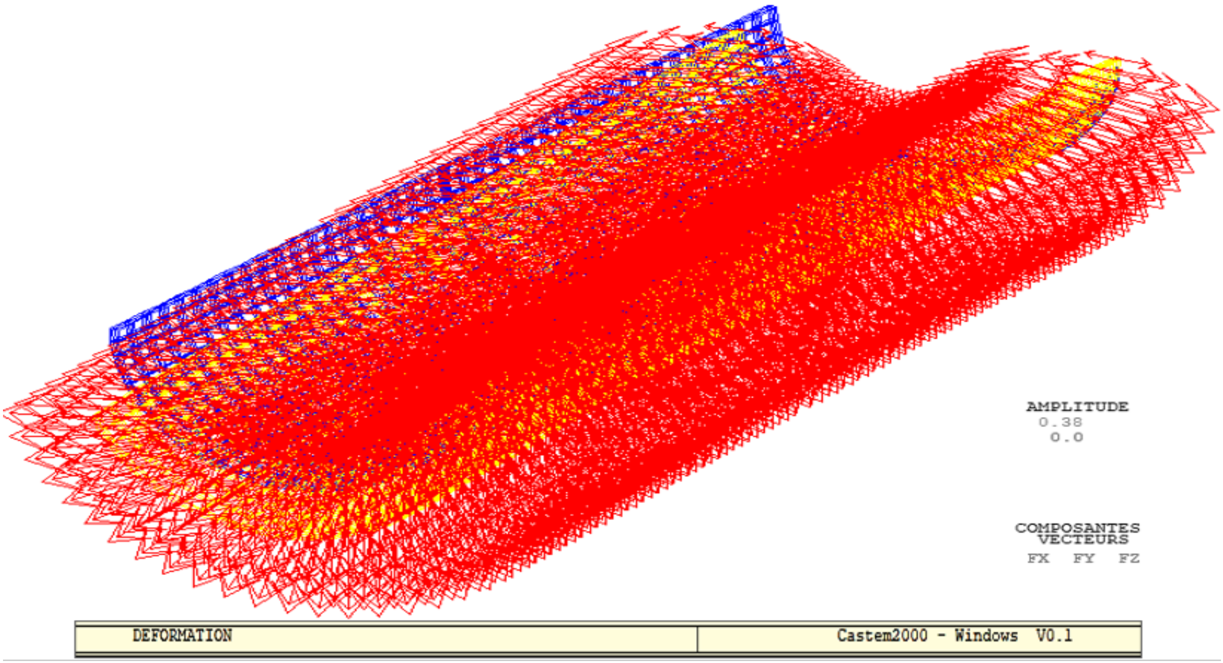

Fig. 6 *Pressure pipe subjected to internal pressure*

3.2 Numerical Simulation Setup and Meshing Strategy

The XFEM method was employed in this study to simulate defect severity in corroded pipes; a defect in the pipe is numerically simulated by an elliptical circumferential external crack.
A commonly used metal in pressure equipment is 16MnR steel, widely applied in pressure vessels, boilers, and pressure pipes, particularly in environments exposed to moderate temperatures. Below are its main mechanical properties [14].

Pipe is characterized by (t / R_i) ratio: t / R_i >0.1: the pipe is considered thick. t / R_i <0.1: the pipe is considered thin. t / R_i =0.1: the pipe has an average thickness. Geometries of cracked pipes under consideration are described using the following parameters: The ratio of the pipe's thickness (t) to its inner radius (t / R_i). The shape parameter (a/c). The defect depth, normalized by the pipe's thickness: (a / t).

The study investigates the elastic-plastic behavior of 16MnR steel (Table 1). Under specific conditions (specimen type, stress state, temperature, etc.), the critical stress intensity factor K_c for 16MnR steel is approximately 90–100 MPa·√m [15]. The corrosion rate is typically dependent on environmental conditions. For 16MnR steel, it is generally estimated to range between 0.1% and 0.3% per year in moderately corrosive environments. In damage models commonly applied to steel, the critical damage (D_c) is typically considered as D_c =0.25[15].

Table 1 *Mechanical characteristics of 16MnR steel*

Young's modulus, E [GPa]	Yield strength, σ_y[MPa]	Poisson's ratio [ϑ]	Strain hardening coefficient, k [MPa]	Strain hardening exponent, **m**
206	345	0.3	800	0.2

A straight pressurized pipe with uniform wall thickness (t) is modeled under uniform corrosion, leading to a homogeneous reduction in wall thickness. An elliptical surface crack is introduced to represent corrosion-induced defect initiation.

Numerical simulations were conducted using the CASTEM 2025 software, employing a coupled XFEM-Level Set approach to simulate crack propagation in pressurized pipes with thickness transitions. Due to geometric and mechanical symmetry, only half of the pipe domain was modeled, reducing computational cost (Fig. 7a–b). The global mesh consists of 9290 standard CUB8 elements (8-node hexahedra with reduced integration), while the region surrounding the semi-elliptical crack is locally refined using 200 enriched XC8R elements equipped with

Int. Journal of Integrated Engineering Vol. 18 No. 3 (2026) p. 63-88

612 Gauss points (Fig.7c), ensuring accurate resolution of stress gradients and crack-tip singularities. This meshing strategy balances computational efficiency with high-fidelity local representation.

Symmetry boundary conditions are applied to constrain translational and rotational degrees of freedom across the plane of symmetry. The material behavior of 16MnR steel is described by an isotropic elasto-plastic constitutive law (Ouglova model [7]) within cracked regions and a kinematic hardening model elsewhere, effectively capturing plastic deformation and strain localization.

Crack geometry and evolution are tracked implicitly through Level Set functions (ψ and φ), while the Stress Intensity Factor (SIF) is computed via the G-theta method, derived from the J-integral, providing values at both the deepest and surface points of the crack. Corrosion-induced wall thinning is incorporated by progressively reducing local thickness based on the spatial distribution of corrosive concentration, thereby modifying mechanical properties locally. This integrated framework enables a precise representation of fracture mechanics in complex geometries, accounting simultaneously for geometric transitions, internal pressure, corrosion degradation, and material nonlinearity.

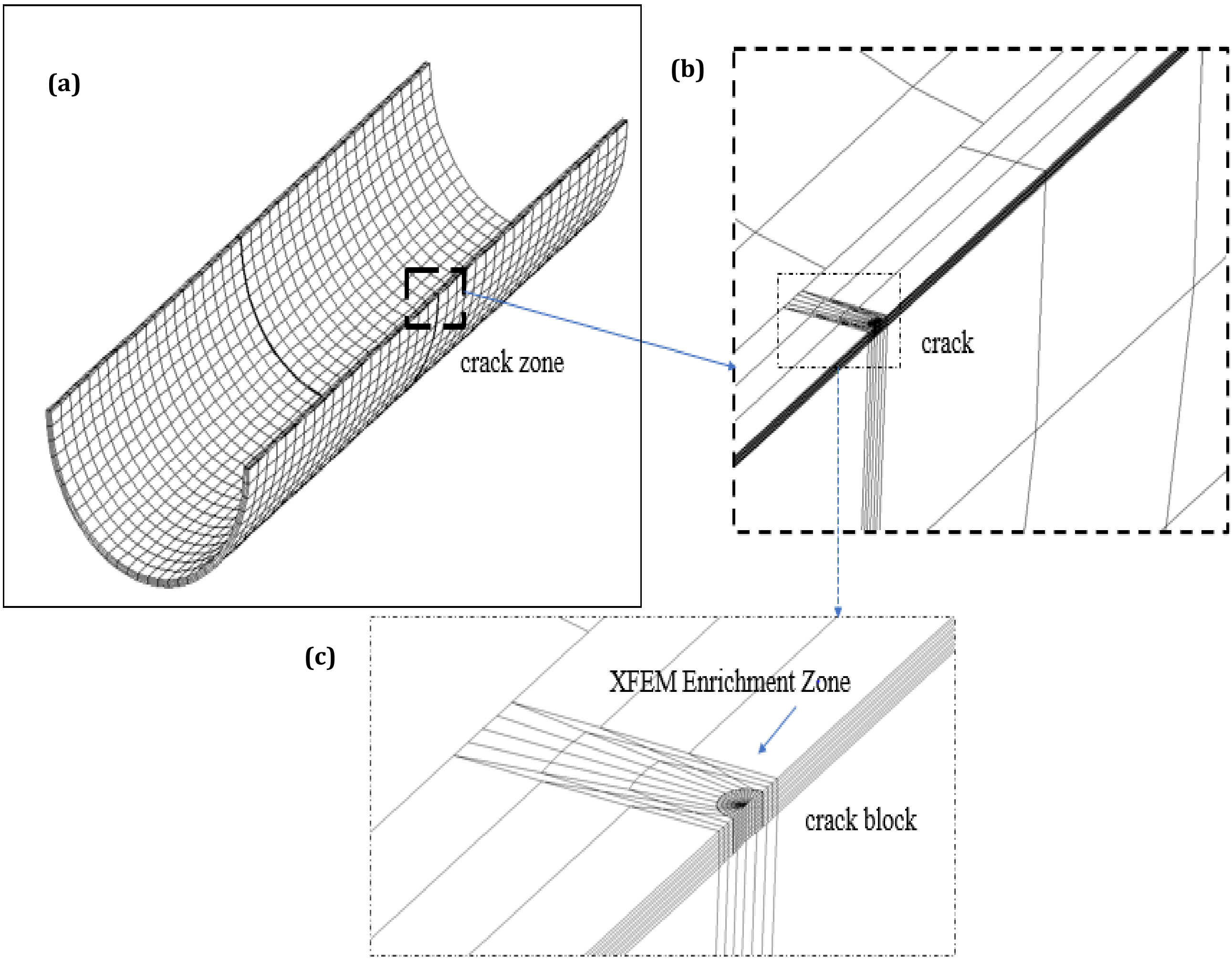

Fig. 7 *Mesh of a half-corroded pipe with superficial crack (a) Overall view of the mesh; (b) Zoom on the crack zone; (c) Zoom on the crack block with XFEM enrichment zone*

4. Results and Discussions

4.1 Validation of the XFEM Code

The CASTEM Program was employed for the modeling and computation. The CASTEM program was employed for the modeling and computation. To verify the validity of the model, the ASME B31G method was used to calculate the ultimate pressure according to Eq. (31), First, the theoretical ultimate pressure, denoted as (P_{cal}), was calculated. Next, the simulated stress (σ) was measured, and the simulated ultimate pressure, (P_{sim}), was deduced. Finally, the theoretical and simulated results were compared to evaluating the accuracy of the model.

Figs. 8–11 present a comparison between the ultimate pressure values calculated theoretically and those obtained from numerical simulations. The ultimate pressure was simulated for a range of parameter values, including (a/t) ratios of 0.1, 0.2, 0.4, 0.6, and 0.8 and (a/c) ratios of 1, 1/2, 1/4, and 1/8. Furthermore, simulations were performed for various pipe types, such as thin-walled pipes (t / R_i <0.1) and thick-walled pipes (t / R_i >0.1). This investigation sheds light on the correctness of the model for a variety of material combinations and geometries. The modeling code is validated by the numerical results, which show a modest deviation from the analytical and semi-empirical values.

The validation of the numerical model is based on a comparison between the simulated ultimate pressure using XFEM-Level Set and the analytical predictions derived from the modified ASME B31G code [13], as given by Eq. (31). This approach is consistent with established practices in pipeline integrity assessment, where simplified analytical formulas are used to benchmark advanced numerical models for cracked components under internal pressure [16]. Specifically, [16] demonstrated through both finite element simulations and experimental tests that the stress intensity factor (K) in internally pressurized cylindrical shells with external semi-elliptical cracks shows excellent agreement with analytical estimates when crack depth-to-thickness ratios (a/t) range from 0.1 to 0.8 and aspect ratios (a/c) vary between 0.125 and 1 — precisely the range considered in this study. The reported deviation in [16] was below 6%, which aligns closely with the observed deviation of less than 5% in this work.

Therefore, the good consistency between the XFEM results and ASME B31G predictions confirms the reliability of the proposed numerical framework for assessing defect severity in complex geometries. This validation enables the extension of the investigation to include corroded pressure equipment with multiple slope designs and thickness transitions.

The (a/t) ratio indicates the depth of the pipeline crack. The (a/c) ratio shows the elongation of the crack along the pipeline wall. Specifically, when a/c=1, the crack is circular; as this ratio decreases (a/c=0.125), the fracture becomes more elongated along the wall, indicating a greater expansion in length relative to its depth.

Figs. 8-11 illustrate how fracture elongation and depth variations affect the ultimate pressure for both thick and thin pipelines. The data indicates that as the crack along the pipeline wall exhibits less elongation, the ultimate pressure increases because the ultimate pressure increases as the (a/c) ratio does.

These results are logical and can be explained by physical and mechanical considerations related to the behavior of pressurized pipelines with cracks. When (a/c) increases, the crack becomes less elongated and tends toward a more compact (circular) shape. A compact crack induces lower stress on the pipeline wall because the stress distribution around the crack is more uniform. This explains why, for larger (a/c) ratios, when the fracture is less elongated, the final pressure rises.

The ultimate pressure in a straight pressurized pipeline falls with increasing (a/t) ratio, as seen in Figs. 8-11. This suggests that the deeper the fracture, the lower the ultimate pressure.

This is justified by the fact that a deeper crack (high (a/t)) reduces the effective thickness of the wall resisting the internal pressure. This weakens the structure, increases the local stresses around the crack, and decreases the pipeline's ability to withstand pressure before failure. As a result, as (a/t) increases, the final pressure decreases. Finally, pipeline resistance improves when the fracture is less elongated (high (a/c)). A deeper fracture (high (a/t)) weakens the pipeline and reduces its ability to withstand high pressures. These results support the use of this modeling code to analyze corroded pipelines with double-slope thickness transitions because they are consistent with fracture mechanics and failure criteria for pressurized materials.

Fig. 12 shows the variation of the relative error between the ultimate pressure calculated using the ASME code [13] formula (Eq. 31) and the values simulated by our numerical model, for a/t ratios between 0.1 and 0.8, a/c ratios between 0.125 and 1, and t/R_i ratios between 0.1 and 0.4. The error (Eq.35) is less than 5%.

$$Re\,l\,ative\ error\ (\%) = \left|\frac{\boldsymbol{P_{cal} - P_{simu}}}{\boldsymbol{P_{cal}}}\right| \times \mathbf{100} \tag{35}$$

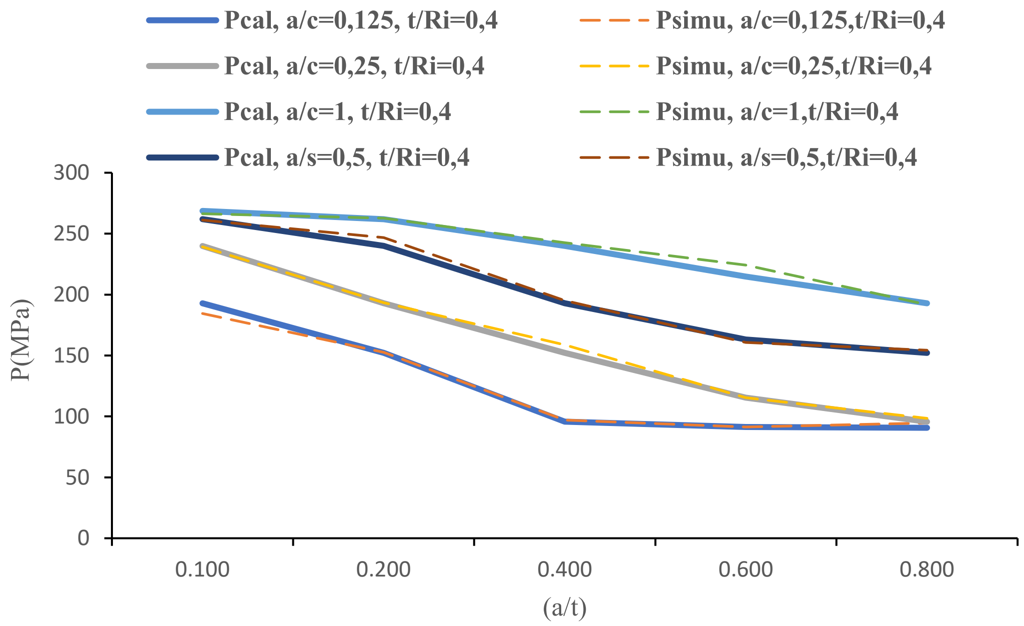

Fig. 8 *Comparison of ultimate pressure values: theoretical calculations vs. XFEM simulation results,* $\boldsymbol{t/R_i = 0.4}$

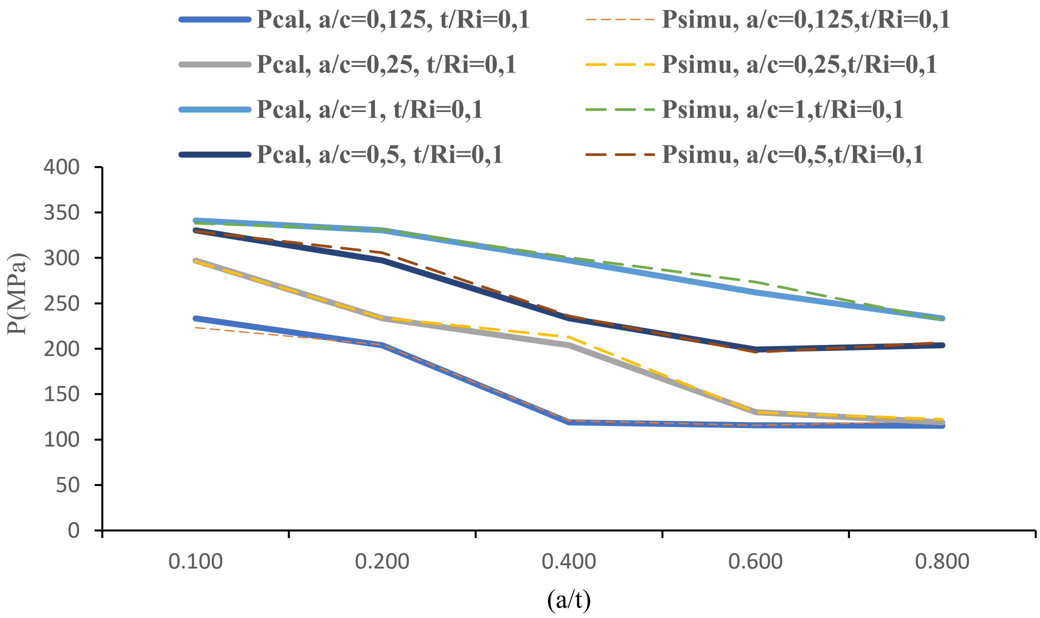

Fig. 9 *Comparison of ultimate pressure values: theoretical calculations vs. XFEM simulation results,* $\boldsymbol{t/R_i = 0.1}$

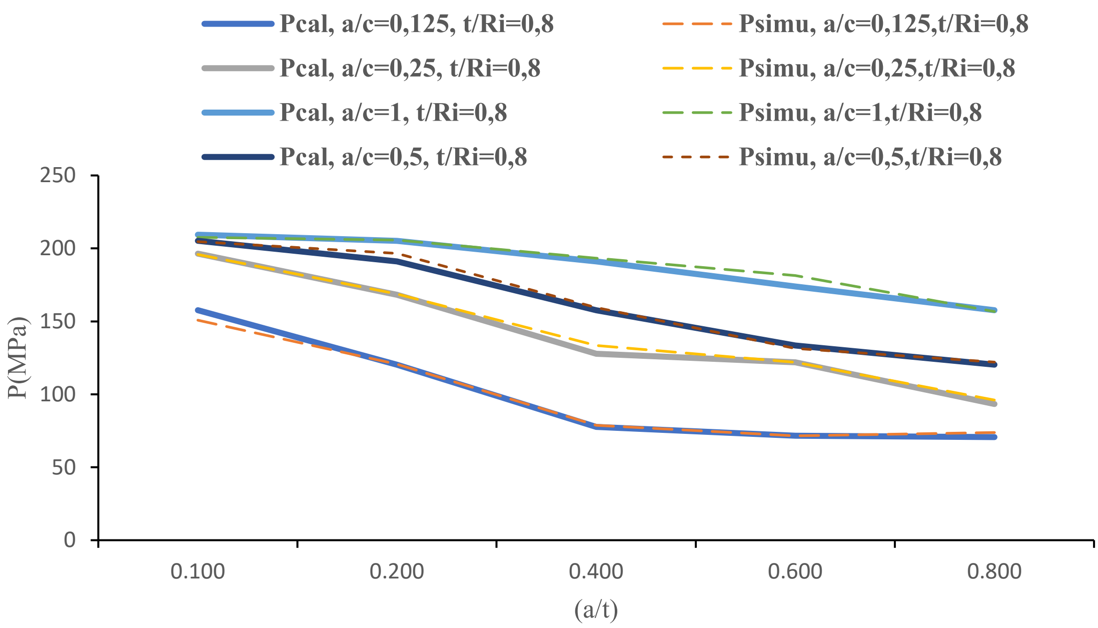

Fig. 10 *Comparison of ultimate pressure values: theoretical calculations vs. XFEM simulation results,* $t/R_i = 0.8$

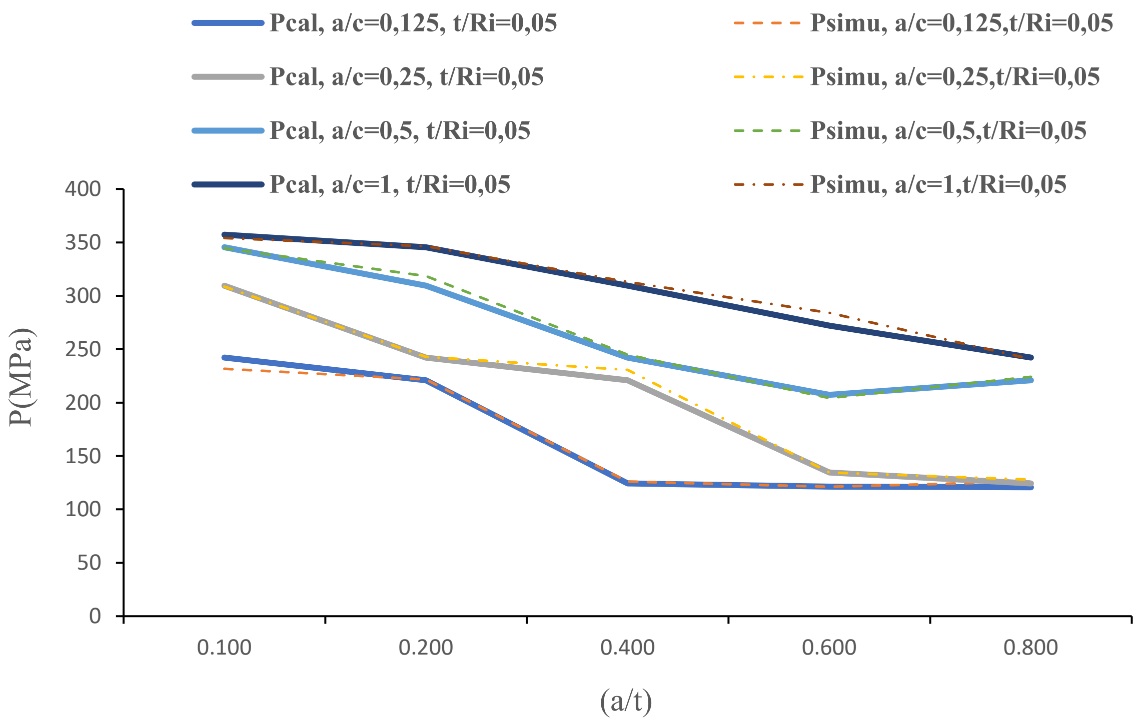

Fig. 11 *Comparison of ultimate pressure values: theoretical calculations vs. XFEM simulation results,* $t/R_i = 0.05$

Int. Journal of Integrated Engineering Vol. 18 No. 3 (2026) p. 63-88

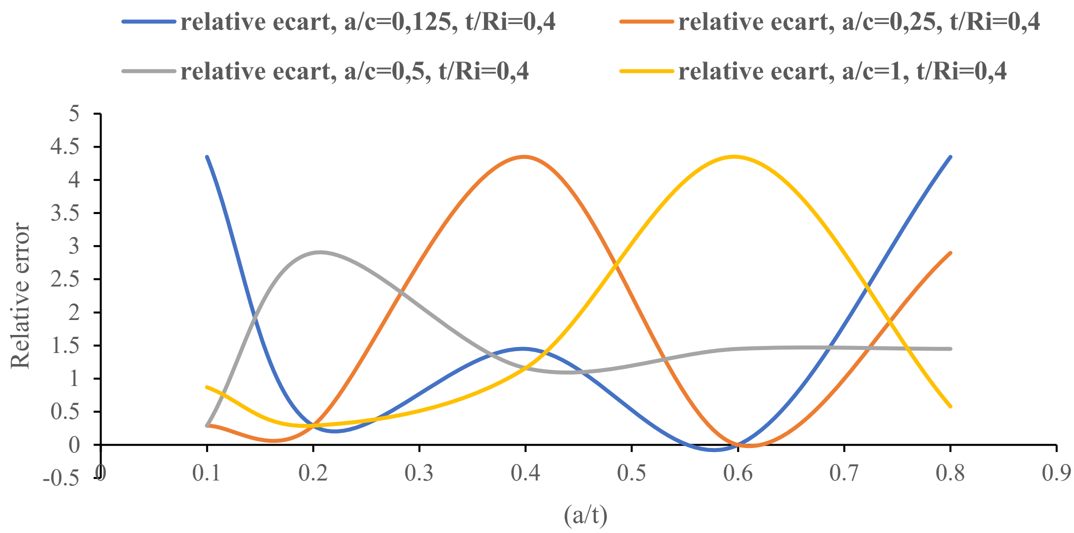

Fig. 12 *Variation of the relative error between ultimate pressure predicted by the ASME B31G analytical model and XFEM-based numerical simulations,* $t/R_i = 0.4$

4.2 Influence of Geometric Parameters of the Corroded Double-Slope Pipe on the SIF Value

In the continuation of the study, the severity of the crack was evaluated through the Stress Intensity Factor (K), calculated using the G-theta method in CASTEM.

A semi-elliptical defect is defined by specific points: the deepest point and the surface point (Fig. 13. a). Typically, assessing (K) at these two locations is sufficient to evaluate the nocivity of the corrosion. At these points (Fig. 13.b), the average (K) value is determined using Eqs. (36-37) [8]:

$$K_{average} = \frac{1}{5}\left(4K_{po\,int\,2} + K_{po\,int\,3}\right) \quad in \quad D \quad point \tag{36}$$

$$K_{average} = \frac{1}{6}\left(K_{po\,int\,4} + 4K_{po\,int\,5} + K_{point6}\right) \quad in \quad S \quad point \tag{37}$$

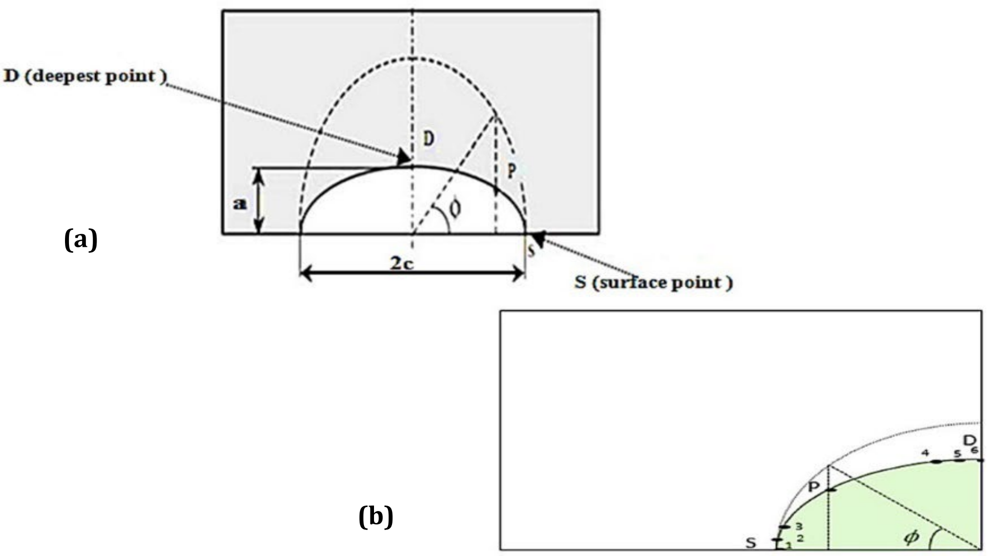

Fig. 13 *Crack (a) Surface point and deepest point of a crack; (b) Definition of average values within the element*

In this part, the severity of the crack in a corroded pipeline with a thickness transition (Fig. 14) will be investigated. Pressure takes values of 10 and 30 Bars.

The study focused on the elastic behavior of 16MnR steel (Table 1-Part 3). The pipes analyzed include thickness transitions, with elliptical cracks assumed to be positioned at the base of the transition on the thinner side of the pipe (Figs. 15-16). A double-slope corroded pipe with an average thickness of (t/R_i=1/10) is modeled. The ratio a/c takes values 1, 0.5, 0.25, and 0.125.

In this study, the geometric parameters (t_1/t), (t_2/t_1), α_1 and α_2 were varied, and their influence on the severity of the crack in a corroded pipeline with a thickness transition was observed.

The ratio (t_1/t) takes the values 1, 1,5, 2, 2.5, 3, 3.5, 4, 4.5, 5, 5.7, 6

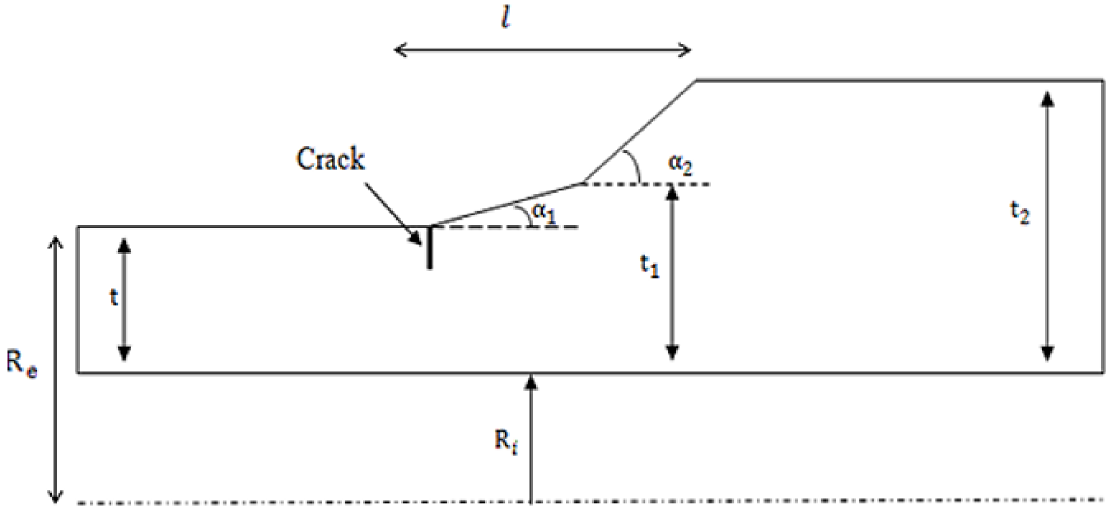

Fig. 14 *Schematic representation of the double-slope pipe geometry with key geometric parameters*

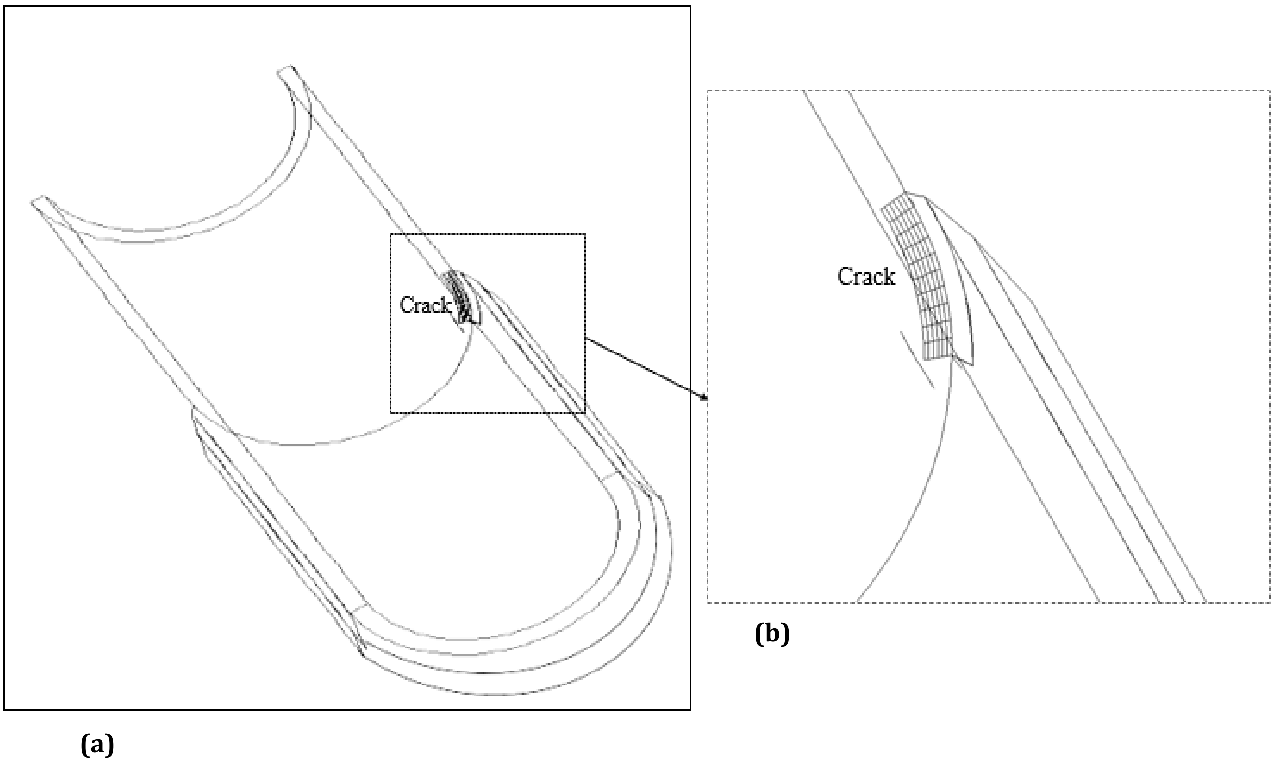

Fig. 15 *Crack in a double-slope pipe (a) 3D mesh of the corroded pipe with an elliptical surface crack located at the first thickness transition; (b) Zoom on the crack in the double-thickness transition zone*

Int. Journal of Integrated Engineering Vol. 18 No. 3 (2026) p. 63-88

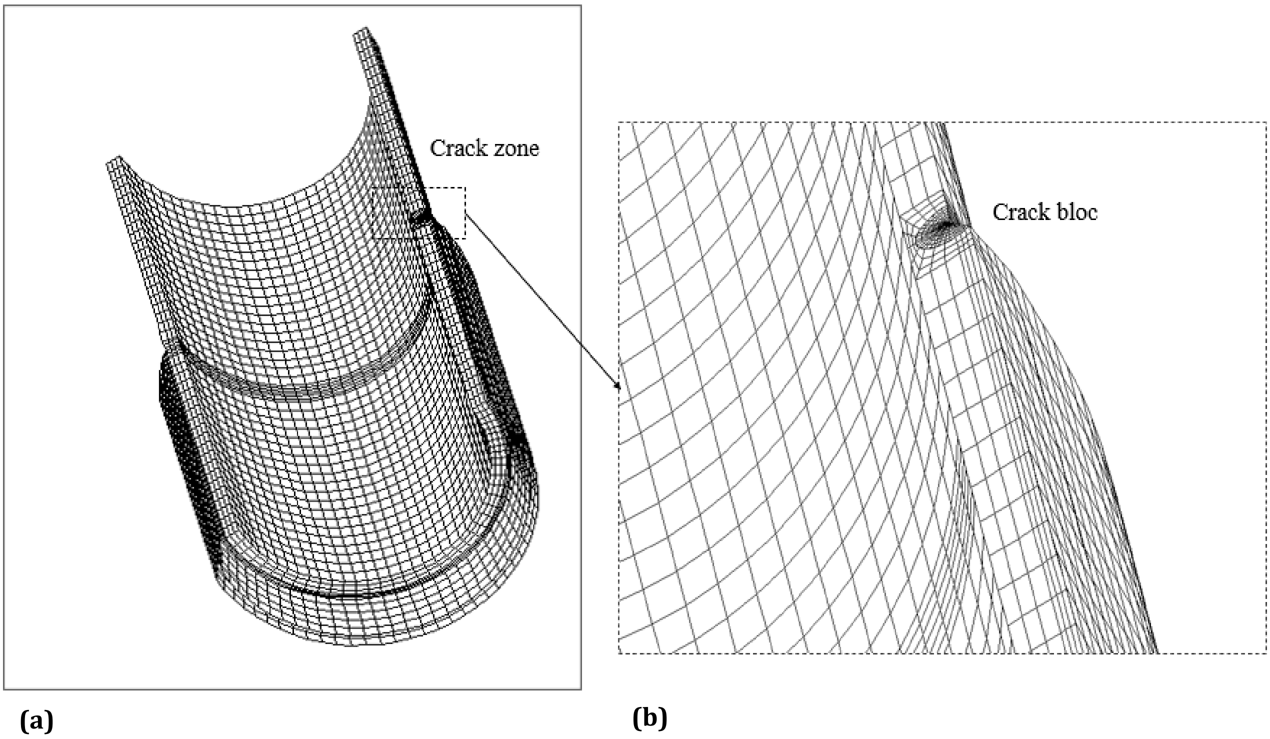

Fig. 16 *Mesh of a double-corroded pipe (a) General view of the mesh in the crack zone; (b) Zoom on the crack*

Figs. 17–18 illustrate the evolution of the SIF values at the deepest and surface points as a function of the geometric ratios of the double-slope corroded pipe. In this study, the angles were fixed at α_1 = 15° and α_2 = 20°, and the pipe has a thickness (t) of 35 mm.

The results show that the primary transition ratio t_1/t dominates stress concentration: when t_1/t increases from 1.5 to 6, the stress intensity factor (K) at the deepest point of the crack increases from 20.4 MPa√m to 105.9 MPa√m, exceeding the critical threshold of 90 MPa√m for 16MnR steel and triggering localized plasticity.

The results show that the stress intensity factor values are higher at the deepest point compared to those measured at the surface point; this can be justified by the fact that, for a corroded pipe subjected to internal pressure, the distribution of stresses varies depending on the geometry of the defect, the depth of the crack, and the wall thickness. In this instance, regions close to the fracture depth endure more stress than the surface, which may be accounted for by several factors:

- Stress concentration at depth: Tensile and compressive stresses are created through the wall thickness of the pipe when internal pressure is applied. Because corrosion has impaired the wall's capacity to sustain internal pressure, the section close to the fracture depth is more susceptible. Because of this, there is greater tension focused in this area, which may cause cracks to spread more widely.

- Internal pressure's effect on surface areas: The surface experiences internal pressure as well, but because the material's resistance to corrosion is less pronounced there, the stresses are less concentrated than in deeper locations. Since the fracture is often not as deep and the material has a greater ability to disperse loads, the surface receives more distributed strains. On the other hand, the depth of the crack, where the wall is weaker and less resistant, is more likely to concentrate stresses.

These findings align with the literature, particularly in subsequent studies demonstrating that the deepest point controls fracture initiation, highlighting the dependence of K on local geometry [17].

Figs. 17–18 also show that the values of the stress intensity factor increase with the rise in the geometry ratios of the double-slope pipe, namely t_1/t and t_2/t_1. As both ratios increase, the ability of the pipe to resist internal pressures changes, leading to higher stress concentrations and, subsequently, higher stress intensity factors. This clarifies why the SIF value rises as the geometric ratios grow.

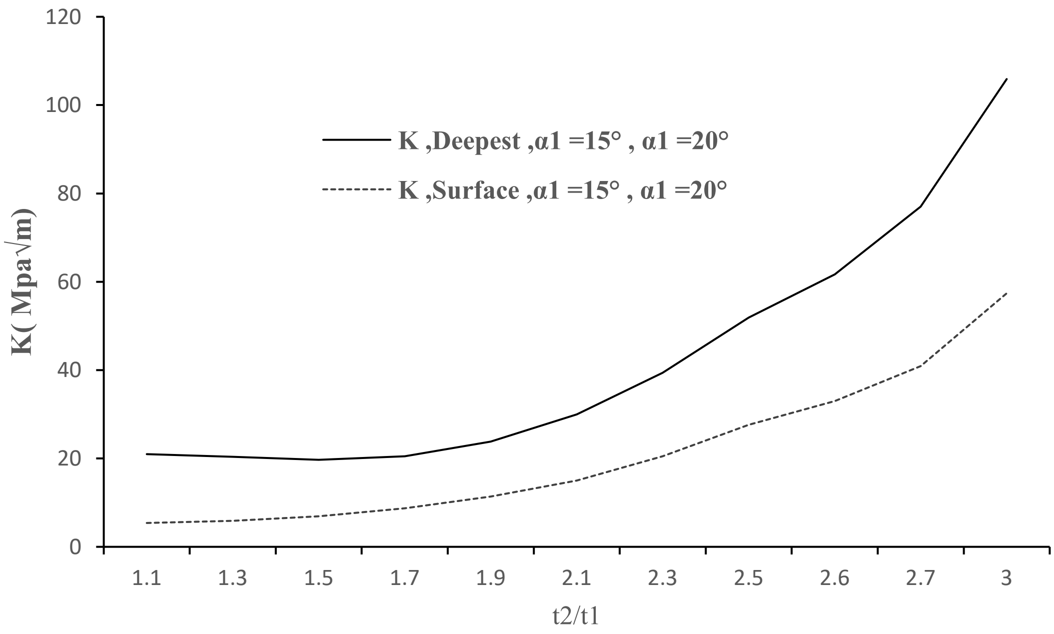

Fig. 17 *Variation of K values with respect to the parameter* (t_2/t_1)

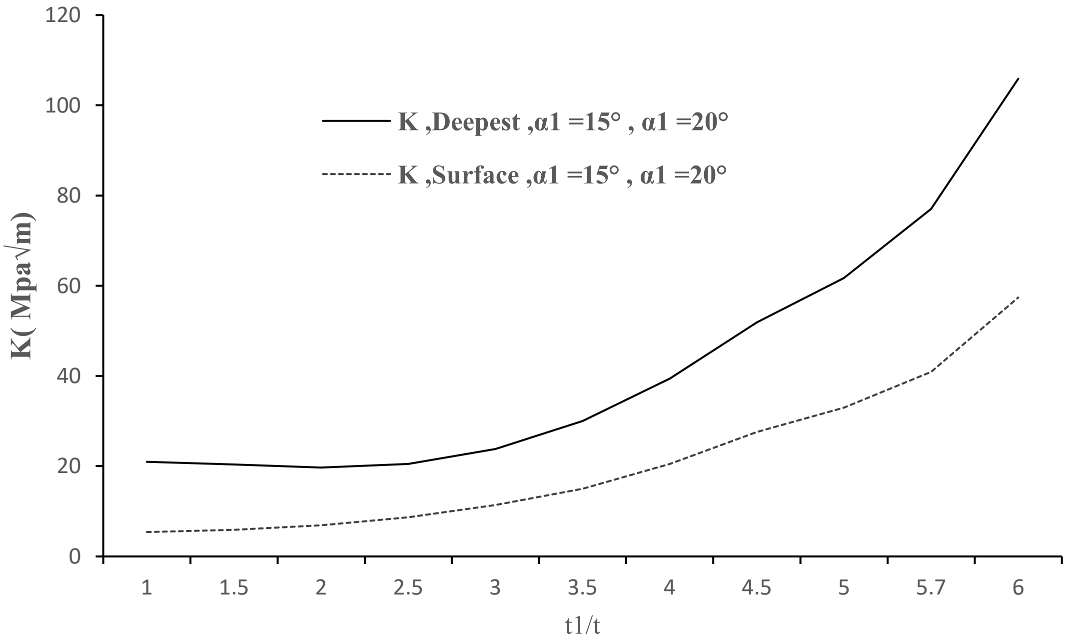

Fig. 18 *Variation of K values with respect to the parameter* (t_1/t)

Figs. 19-20 illustrate the combined influence of geometric parameters on the stress intensity factor (K) at the deepest point and surface point of a semi-elliptical crack in a corroded pipe with double-slope thickness transitions, under a constant internal pressure of 15 bars and fixed transition angles α_1 = 15°, α_2 = 20°. The comparative analysis reveals that the primary transition ratio t_1/t exerts a dominant influence on defect severity: K generally increases with t_1/t, which is consistent with the reduction in local stiffness due to progressive wall thinning.

A notable phenomenon appears in Fig.19: the curves corresponding to t_2/t_1 = 1.5 and t_2/t_1 = 2.5 intersect for $t_1/t \in [4, 4.5]$. More precisely:

- For $t_1/t < 4$, the curve associated with $t_2/t_1 = 1.5$ lies below that for $t_2/t_1 = 2.5$.
- For $t_1/t > 4.5$, the curve for $t_2/t_1 = 1.5$ surpasses that for $t_2/t_1 = 2.5$.

This intersection is explained by a shift in dominance between the stress concentration mechanisms:

- For low values of t_1/t (a sharp transition), the first slope dominates the mechanical response; the effect of t_2/t_1 is marginal.
- For higher values of t_1/t (a less abrupt transition), the second transition begins to significantly influence stress redistribution. A high value of t_2/t_1 (e.g., 2.5) means the post-transition section is even thinner, reducing the overall structural stiffness and enabling better stress dissipation, leading to a relative decrease in K compared to an intermediate value of t_2/t_1 (e.g., 1.5).

In contrast, this phenomenon is not observed at the surface point (Fig. 18), where the curves remain well ordered: For all values of t_1/t, the curve for $t_2/t_1 = 4.5$ remains above those for $t_2/t_1 = 2.5$ and $t_2/t_1 = 1.5$.

This is explained by the geometric localization of the crack:

- At the deepest point, the crack is located at the base of the first transition, where the wall is thinnest. The second transition, located farther away, therefore has an indirect and nonlinear impact on stress concentration — hence the intersection.
- At the surface point, the crack is closer to the outer surface, where the effects of the second transition are less sensitive. Moreover, stresses are more uniformly distributed there, making the influence of t_2/t_1 additive and monotonic — no inversion is possible.

Thus, the intersection of the curves reflects a shift in the hierarchy of geometric effects: the first transition imposes stress concentration at low t_1/t, while the second transition modifies the structural response at higher t_1/t, highlighting the importance of considering both parameters jointly to accurately assess defect nocivity in double-slope pipes.

This non-monotonic behavior, characterized by the crossing of SIF curves for different t_2/t_1 ratios, is consistent with the stress redistribution mechanisms reported by Chen & Zhang (2020) [18] in multi-step cylindrical components under internal pressure. They demonstrated that as the primary transition becomes less abrupt, the secondary transition begins to govern the global stiffness, leading to a stress-relieving effect that can reduce the SIF for higher t_2/t_1 values.

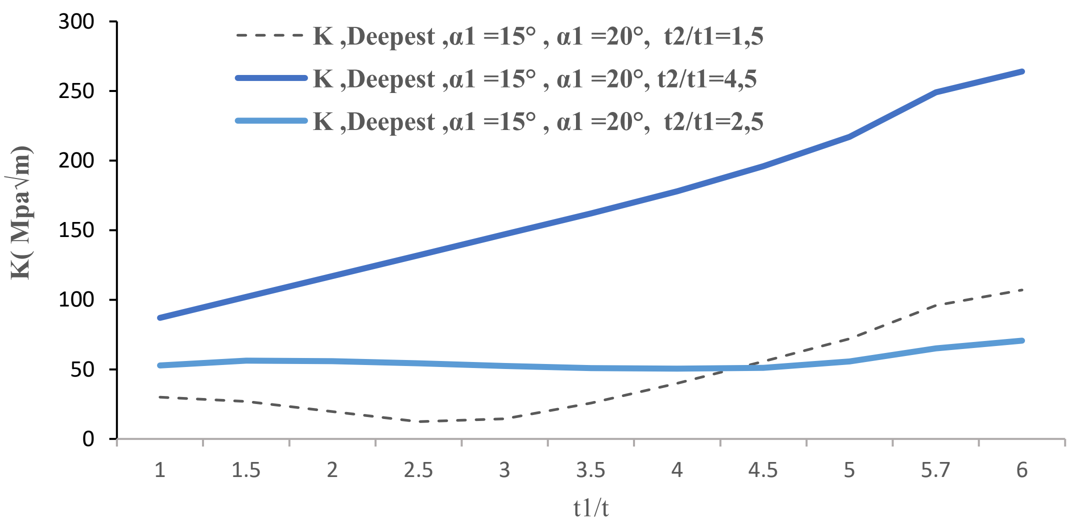

Fig. 19 *Variation of K values with respect to the parameter* (t_1/t), *deepest point,* (t_2/t_1) *values are fixed*

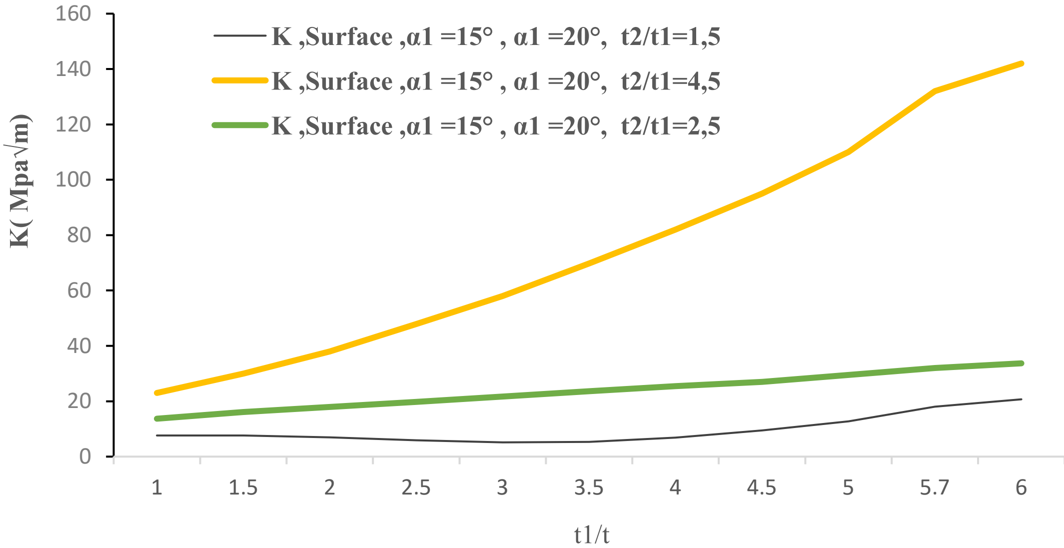

Fig. 20 *Variation of K values with respect to the parameter* $(\boldsymbol{t_1/t})$*, surface point,* $(\boldsymbol{t_2/t_1})$ *values are fixed*

Figs. 21 - 22 illustrate the evolution of the stress intensity factor (K) at the surface point and the deepest point of a semi-elliptical crack in a corroded pipe with double-slope thickness transitions, as a function of the geometric ratio t2/t1, with the first transition ratio t1/t held constant. These figures reveal that the influence of the second transition on defect severity is significantly less than that of the first transition, a fundamental result for the design and inspection of pipelines. For each fixed value of t1/t (1.5, 2.5, or 4), K increases slightly with t2/t1 , but this increase remains modest and does not exceed the critical plasticity threshold for 16MnR steel. This low sensitivity is explained by the geometric localization of the crack: as shown in Fig. 13, the crack is positioned at the base of the first transition, where the wall thickness is minimal; the second transition, located farther away, therefore has a limited impact on local stress concentration around the crack. In contrast, an increase in t1/t —which locally reduces the pipe's stiffness—leads to a significant amplification of K, pushing the material beyond the elastic domain and highlighting the predominant role of the first transition in stress management. These findings have major practical implications: non-destructive inspections must prioritize areas near the first transition, while the second transition can be considered secondary in life prediction models, except in specific cases where it is very close to the crack.

Unlike the previous section, where the first transition ratio t1/t was varied, this analysis fixes t1/t at constant values (1.5, 2.0, and 4.0) while systematically varying the second transition ratio t2/t1 (1.5, 2.3, and 4.0). The stress intensity factor (K) is evaluated at both the surface and deepest points of the semi-elliptical crack under an internal pressure of 15 bar. The results are presented in Figs. 19 - 20 demonstrate that the second transition parameter t2/t1 exerts a significantly weaker influence on defect severity compared to the primary transition (t1/t). Although increasing t2/t1 leads to a marginal rise in K values, this effect remains well below the critical threshold for plasticity in 16MnR steel. In contrast, the first transition parameter t1/t governs the overall stress concentration, as its variation drastically alters the local wall thickness and stiffness near the crack tip—the primary zone of stress amplification. The minimal impact of t2/t1 is physically justified by the spatial localization of the defect: since the crack is positioned at the base of the first transition, the second transition lies too far downstream to significantly perturb the stress field around the crack front. Consequently, even when t2/t1 increases—leading to a thinner post-transition section—the resulting structural softening occurs too remotely to substantially influence the K values at the crack site. This confirms that, in double-slope corroded pipes, the first transition is the dominant geometric feature controlling defect severity, while the second transition can be considered secondary in failure assessment models, provided the crack remains localized near the primary transition zone.

The observed trends in stress intensity factor (K) are consistent with fundamental principles of linear elastic fracture mechanics (LEFM), which state that geometric discontinuities near a crack tip significantly alter the local stress field. In particular, thickness transitions act as stress concentrators, and their proximity to the crack governs the magnitude of K [8]. Moreover, the dominance of the first thickness transition aligns with prior studies on

Int. Journal of Integrated Engineering Vol. 18 No. 3 (2026) p. 63-88

stepped cylindrical components under internal pressure, where the nearest geometric perturbation to the crack was shown to control the stress intensity factor [8, 19].

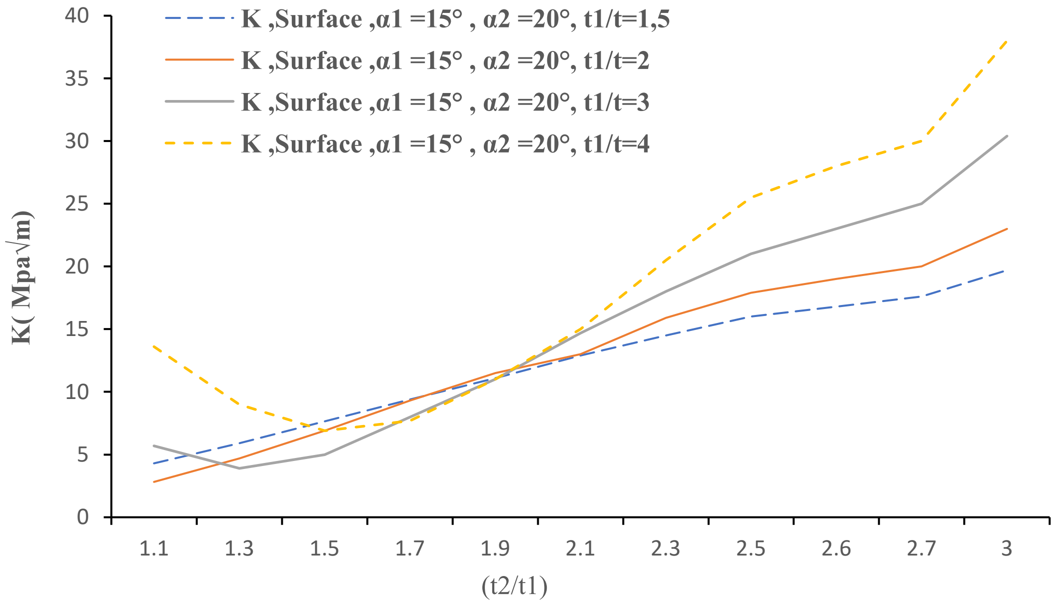

Fig. 21 *Variation of K values with respect to the parameter* $(\boldsymbol{t_2/t_1})$*, surface point,* $(\boldsymbol{t_1/t})$ *values are fixed,* $\boldsymbol{\alpha_1}$ *=15°and* $\boldsymbol{\alpha_2}$*= 20°*

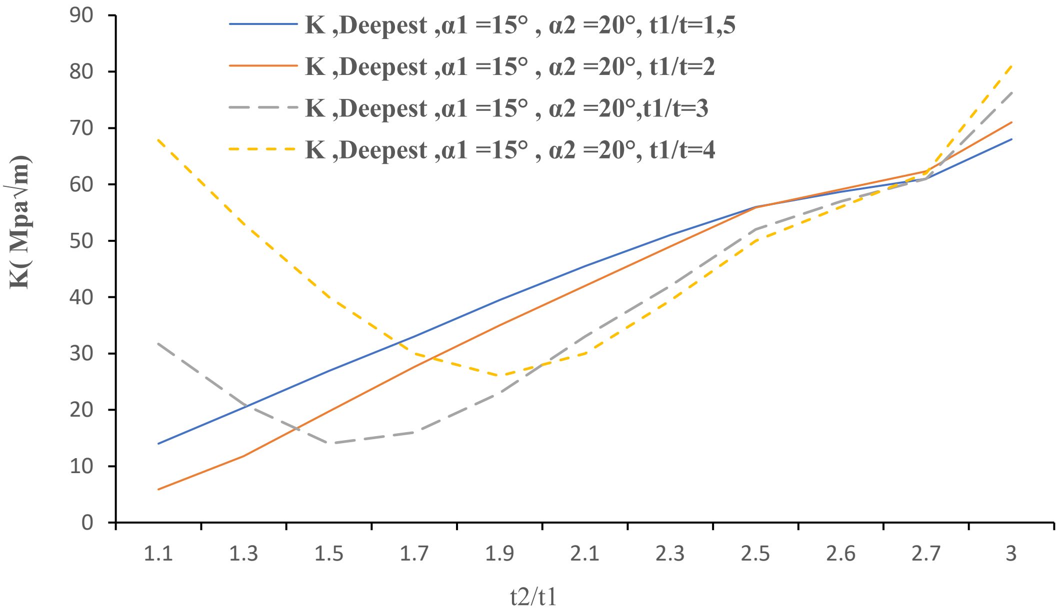

Fig. 22 *Variation of K values with respect to the parameter* $(\boldsymbol{t_2/t_1})$*, deepest point,* $(\boldsymbol{t_1/t})$ *values are fixed,* $\boldsymbol{\alpha_1}$ *=15°and* $\boldsymbol{\alpha_2}$*= 20*

4.3 Influence of Slopes and Corrosion Rate on Defect Severity in the Corroded Pipe with Thickness Transition

Based on the previous results, it was observed that the parameter (t_1/t) has a more significant impact on defect severity compared to the second transition parameter (t_2/t_1), Therefore, in this section, the variation of (t_1/t) is considered, and the values of the angles for assessing the defect severity in the corroded pipe with a double transition.

The graphs of Figures 23-24 illustrate the influence of the two slopes of the corroded pipe on defect severity at both the depth and surface points, as a function of the ratio (t_1/t).

The results indicate that the values of (K) increase with the rise in the ratio (t_1/t), exceeding the critical stress intensity factor of elasticity at both the depth and surface points. Additionally, they show that reducing the slope values increases the defect severity in a corroded double-slope pipe. To better visualize these findings, the influence of each slope on defect severity is analyzed separately in the following section.

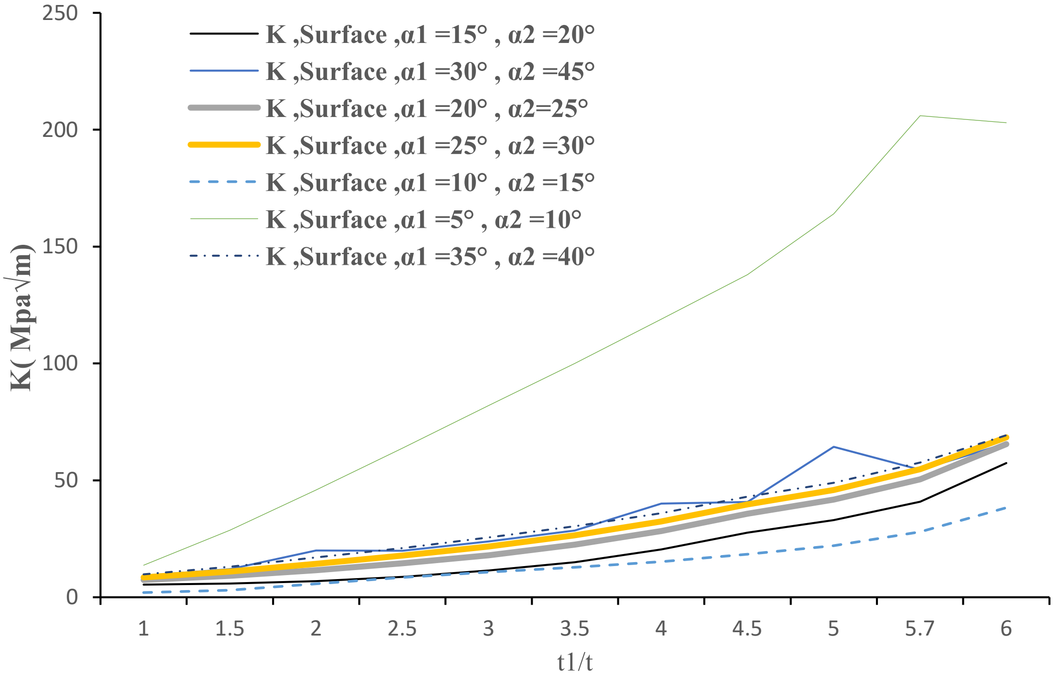

Fig. 23 *Variation of K values with respect to the parameter* $(\boldsymbol{t_1/t})$ *and double-slope variation, surface point*

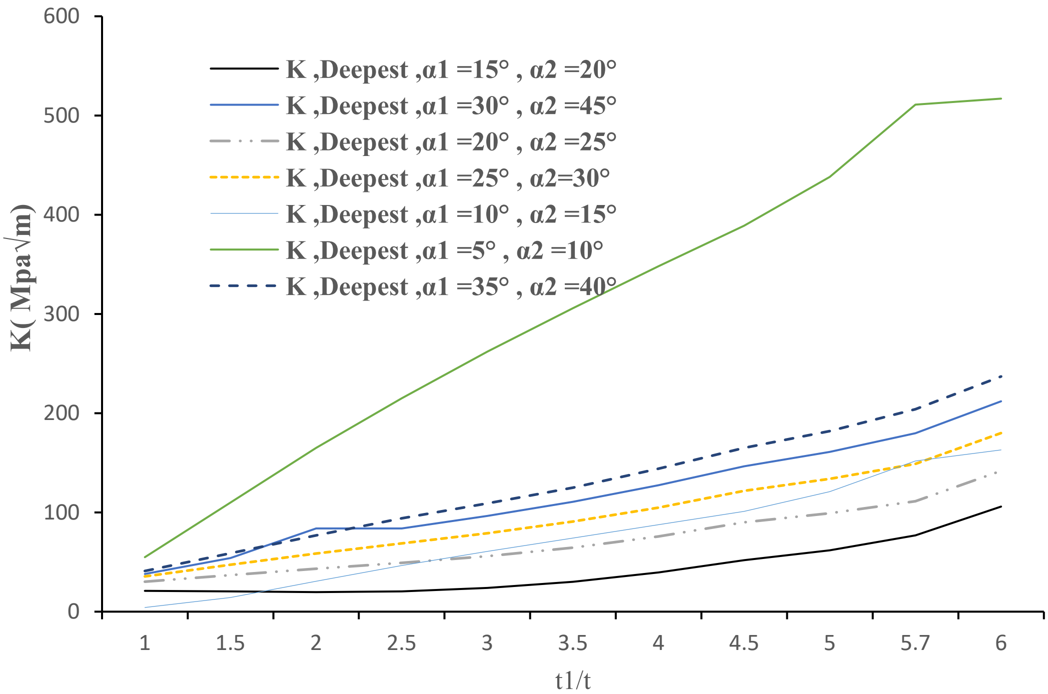

Fig. 24 *Variation of K values with respect to the parameter* $(\boldsymbol{t_1/t})$ *and double-slope variation, deepest point*

Int. Journal of Integrated Engineering Vol. 18 No. 3 (2026) p. 63-88

At this stage, the slope values were varied, while the other parameters of the double-slope pipe were kept constant. Fig. 25 shows the evolution of the values of (K) as a function of the first slope (α_1) for an internal pressure of 15 bars, with fixed values of $\boldsymbol{\alpha_2}$=15°, (t_1/t) =(t_2/t_1)=1.5. Fig. 26 illustrates the evolution of the values of (K)as a function of the second slope α_2 under the same internal pressure of 15 bars and fixed values of $\boldsymbol{\alpha_1}$=15°, (t_1/t)=(t_2/t_1)=1.5.

The results confirm that the second slope has a minor influence on the defect severity in a corroded pipe. The variation in (K) values remains constant and takes values significantly below the elastic limit. In contrast, the first slope $(\boldsymbol{\alpha_1})$ has a noticeable impact on defect severity, particularly for small $(\boldsymbol{\alpha_1})$ values. In this case, (K) reaches high values exceeding the critical stress intensity factor, causing the material behavior to transition from elasticity to plasticity. An increase in the first slope (α_1) results in a decrease in (K) values, allowing the material to regain its elastic behavior. However, when the slope (α_1) continues to increase further, the defect severity also increases.

The justification is based on the principles of structural mechanics and crack propagation in materials subjected to internal stresses: A small value of (α_1) generates a high concentration of localized stresses, which amplifies the stress intensity factor (K) beyond the critical limit. This leads to plastic behavior in the material in that area, as the stresses exceed its elastic limit. When (α_1) increases, the local geometry becomes more favorable for a uniform distribution of stresses, reducing the severity of the defect and allowing the material to regain its elastic behavior. The second slope (α_2) has a less significant effect because it is farther from the defect-affected area (in the first transition). Variations in (α_2) do not cause notable changes in the stress distribution around the crack, which explains why (K) remains constant and below the critical threshold.

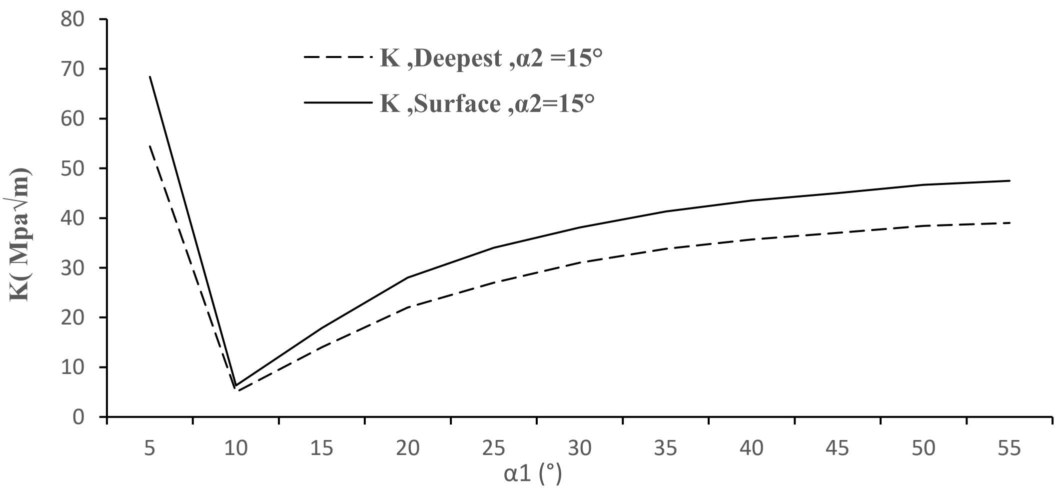

Fig. 25 *Evolution of K values as a function of the first slope* $\boldsymbol{\alpha_1}$*,* $\boldsymbol{\alpha_2}$*=15°,* $(\boldsymbol{t_1/t})$ *=* $(\boldsymbol{t_2/t_1})$*=1.5*

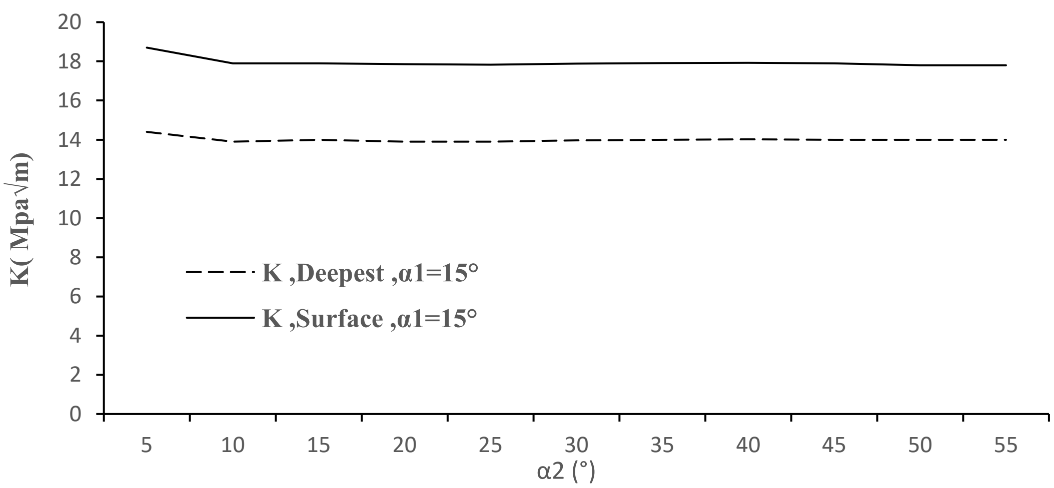

Fig. 26 *Evolution of K values as a function of the second slope* $\boldsymbol{\alpha_2}$*,* $\boldsymbol{\alpha_1}$*=15°,* $(\boldsymbol{t_1/t})$ *=* $(\boldsymbol{t_2/t_1})$*=1.5*

At this stage, the variation in K values was simulated as a function of the cumulative metal loss, (t_c) for a cracked pipe with a double-thickness transition and uniform corrosion. The slope values and the geometric ratios of the two transitions were held constant.

Note that in Fig. 27, the abscissa represents the cumulative metal loss, (t_c) , not the annual corrosion rate. For a typical corrosion rate of 0.1–0.3 %/year, a cumulative loss of 5 % to 30 % corresponds to service durations of approximately 17 to 100 years, covering the realistic operational lifespan of industrial pipelines.

Fig. 27 illustrates the evolution of the stress intensity factor (K) as a function of (t_c) under different internal pressures (15, 30, and 40 bar). The results confirm that K increases with rising internal pressure, while showing a consistent trend of slight reduction as (t_c) increases — an effect attributed to crack tip blunting, a well-documented phenomenon in corroded steel structures [5, 15].

For instance, at 15 bars, K at the deepest point decreases from 14.6 MPa√m at (t_c) =5% to 9.5 MPa√m at tc =60%, reflecting a gradual decline of approximately 35%.

This behavior aligns with earlier findings (Figs. 25–26): the first slope exerts a dominant influence on defect severity in uniformly corroded pipes with dual-slope profiles and semi-elliptical cracks. This is because the most pronounced wall thinning occurs at the first transition, increasing the local crack-to-wall thickness ratio and thereby amplifying stress concentration around the crack tip. In contrast, the second slope induces minimal changes in residual geometry due to its less severe thinning, resulting in a negligible impact on K.

Thus, although K remains relatively stable during early corrosion stages, it exhibits a moderate decrease at advanced stages — a trend illustrating how the initial slope governs defect severity, while the slight reduction in K reflects crack tip blunting, as previously observed in 16MnR steel under uniform corrosion [15] and in environmentally assisted cracking scenarios [5].

In conclusion, it is entirely reasonable to conclude that the first slope significantly elevates K, whereas the second slope has only a marginal effect — underscoring the critical role of local geometry, particularly noticeable wall thinning, in driving stress concentration at the semi-elliptical crack tip.

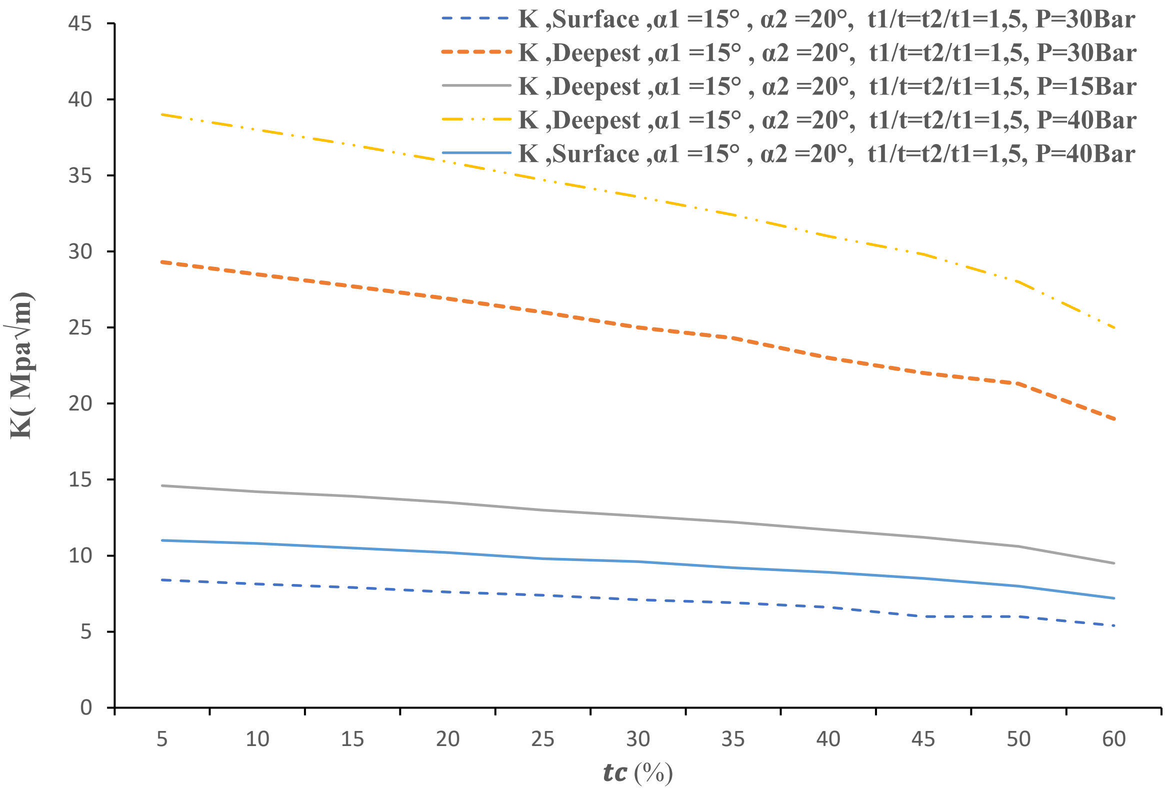

Fig. 27 *Evolution of K values as a function of the corrosion rate* t_c

5. Conclusion

This study demonstrates that in double-slope corroded pipes, the severity of semi-elliptical cracks is primarily governed by the first thickness transition located immediately adjacent to the defect. Due to the localized wall thinning it induces, this transition significantly concentrates stresses around the crack, leading to a substantial increase in the stress intensity factor and, in many cases, exceeding the critical plasticity threshold of 16MnR steel.

In contrast, the second transition, being farther from the defect, exerts only a marginal influence on defect severity, even when highly pronounced. Furthermore, the effect of uniform corrosion manifests as a slight reduction in the stress intensity factor at advanced stages, attributed to crack tip blunting. These findings underscore the dominant role of local geometry — particularly wall thinning at the first transition — in determining defect severity. The numerical approach coupling XFEM, Level Set techniques, and a Fick-based corrosion model has proven robust and reliable, paving the way for future extensions incorporating cyclic loading, thermomechanical effects, or localized corrosion patterns to enable even more realistic assessments of residual lifetime in industrial pipelines.

Acknowledgement

We would like to express our appreciation for the support provided by all parties directly or indirectly involved in this research. We also thank our colleagues and collaborators for their support and assistance throughout the research process.

Conflict of Interest

The authors declare that there is no conflict of interest regarding the publication of the paper.

Author Contribution

The authors confirm contribution to the paper as follows: ***study conception and design****: Salmi Houda;* ***analysis and interpretation of results****: Salmi Houda, Lifi Houda, Lamarti Amal;* ***draft manuscript preparation****: Salmi Houda, Hachim Abdelilah, Khalid El Hadl. All authors reviewed the results and approved the final version of the manuscript.*

References

[1] H. M. Farh, M. E. A. Ben Seghier, R. Taiwo & T. Zayed (2023) Analysis and ranking of corrosion causes for water pipelines: A critical review, npj Clean Water, 6(1), 65, https://doi.org/10.1038/s41545-023-00275-5

[2] M. Makuch, S. Kovacevic, M. R. Wenman & E. Martínez-Pañeda (2024) A microstructure-sensitive electro-chemo-mechanical phase-field model of pitting and stress corrosion cracking, Corrosion Science, 232, 112031, https://doi.org/10.1016/j.corsci.2024.112031

[3] A. H. Kherief Nacereddine, O. Kholai, M. Chekired, M. Kadja & T. H. Mai (2024) Numerical simulation of laminar flow of a non-Newtonian bentonite solution in a horizontal pipe, Journal of Computational Applied Mechanics, 55(4), 552–566, https://doi.org/10.22059/jcamech.2024.371990.965

[4] L. Oger (2017) Corrosion sous contrainte et fragilisation par l'hydrogène d'alliages d'aluminium de la série 7xxx (Al-Zn-Mg): Identification des paramètres microstructuraux critiques pilotant l'endommagement à l'échelle locale, Doctoral dissertation, Institut National Polytechnique de Toulouse, https://theses.hal.science/tel-04228477/file/OGER_Loic.pdf

[5] A. Turnbull (2014) Corrosion pitting and environmentally assisted small crack growth, Proceedings of the Royal Society A: Mathematical, Physical and Engineering Sciences, 470(2169), 20140254, https://doi.org/10.1098/rspa.2014.0254

[6] Ouglova, A. Raharinaivo, Y. Berthaud, I. Petre-Lazar & H. Boukhenfouf (2005) Numerical simulation of potential distribution due to the corrosion of reinforcement in concrete structures, Materials and Structures, 38, 711–719, https://doi.org/10.1007/BF02484316

[7] A. Ouglova, Y. Berthaud, F. Foct, M. François, F. Ragueneau & I. Petre-Lazar (2008) The influence of corrosion on bond properties between concrete and reinforcement in concrete structures, Materials and Structures, 41, 969–980, https://doi.org/10.1617/s11527-007-9298-x

[8] H. Salmi, K. El Had, H. El Bhilat & A. Hachim (2019) Numerical analysis of the effect of external circumferential elliptical cracks in transition thickness zone of pressurized pipes using XFEM, Journal of Applied and Computational Mechanics, 5(5), 861–874, https://doi.org/10.22055/jacm.2019.28043.1452

[9] H. Salmi, A. Hachim, H. El Bhilat & K. El Had (2020) Numerical modeling and comparison study of elliptical cracks effect on the pipes straight and with thickness transition exposed to internal pressure, using XFEM in elastic behavior, Journal of Computational & Applied Research in Mechanical Engineering, 10(1), 229–244, https://doi.org/10.22061/JCARME.2019.4050.1488

[10] G. Zumpicchiat (2015) Modélisation numérique de la diffusion-corrosion des alliages de zirconium, Doctoral dissertation, Université Paris-Sud, https://www.researchgate.net/profile/Guillaume-Zumpicchiat/publication/295121741_Finite_element_modeling_of_zirconium-based_alloys_corrosion/links/57bab0ec08ae6f17376855a6/Finite-element-modeling-of-zirconium-based-alloys-corrosion.pdf

[11] C. Berriet & J. Chambert (2019) Analyse d'un cylindre à paroi mince sous pression: Un support simple de montée en compétences, Congrès Français de Mécanique, https://hal.science/hal-02376936/

[12] Salmi, H., El Had, K., El Bhilat, H., Hachim, A. (2020). Numerical Study of SIF for a Crack in P265GH Steel by XFEM. In: Dos Santos, S., Maslouhi, M., Okoudjou, K. (eds) Recent Advances in Mathematics and Technology, Applied and Numerical Harmonic Analysis, Birkhäuser, Cham. https://doi.org/10.1007/978-3-030-35202-8_6

[13] M. J. Rosenfeld (2020) Transportation pipelines, including ASME B31.4, B31.8, B31.8S, B31G, and B31Q codes, in Companion Guide to the ASME Boiler and Pressure Vessel and Piping Codes, vol. 2, https://doi.org/10.1115/1.861981_ch37

[14] Y. Yingxia, H. Bolin, L. Jing, C. Zhaoxia & M. Hua (2015) Surface plastic deformation and nanocrystallization mechanism of welded joint of 16MnR steel treated by ultrasonic impact, Materials Science, 21(4), 612–615, https://doi.org/10.5755/j01.ms.21.4.9563

[15] Y.-P. Cao, H. Hui, F.-Z. Xuan, Y.-B. He & H. Li (2013) A new calibration approach to Beremin's parameters: Application to 16MnR steel, Paper presented at the 22nd Conference on Structural Mechanics in Reactor Technology (SMiRT 22), San Francisco, CA, USA, August 18–23, https://repository.lib.ncsu.edu/server/api/core/bitstreams/31608a90-876f-4d57-a224-7cec36cd145d/content

[16] H. Moustabchir, J. Arbaoui, Z. Azari, S. Hariri & C. I. Pruncu (2017) Experimental/numerical investigation of mechanical behaviour of internally pressurized cylindrical shells with external longitudinal and circumferential semi-elliptical defects, Alexandria Engineering Journal, 56(4), 679–688, https://doi.org/10.1016/j.aej.2017.05.022

[17] Anderson, T. L., & Anderson, T. L. (2005). Fracture mechanics: fundamentals and applications. CRC press. https://www.taylorfrancis.com/books/mono/10.1201/9781420058215/fracture-mechanics-ted-anderson-anderson

[18] Huang, C., Zhang, J., Wang, F., & Di, C. Y. (2022). Restoration of ultimate strength of dented hemispheres under external hydrostatic pressure. China Ocean Engineering, 36(3), 500-507. https://doi.org/10.1007/s13344-022-0043-6

[19] Saffih & S. Hariri (2006) Numerical study of elliptical cracks in cylinders with a thickness transition, International Journal of Pressure Vessels and Piping, 83, 35–41, https://doi.org/10.1016/j.ijpvp.2005.10.002